MASTER THESIS

SINGLE-SHOT CARS IMAGING OF NEAR-WALL TURBULENT REACTING FLOWS

by

Jan Karim El Sioufy

Name	**Std. number**	**Email address**
Karim El Sioufy	4192729	j.k.elsioufy@student.tudelft.nl

Date of delivery: March 26, 2020

Delft University of Technology

CONTENTS

ABSTRACT

This master thesis investigates the assessment of Flame-Wall Interaction using 1D broadband RCARS thermometry. Flame-Wall Interactions (FWI) have been shown to adversely effect combustion processes in terms of both efficiency and maximum performance. Heat and momentum losses cause incomplete combustion and allow for unburnt hydrocarbons (UHCs) and unoxidised radicals such as carbon monoxide to leave a combustion engine. This is not accurately represented within presently used combustion models, which raises the need for accurate data on essential combustion parameters, such as temperature, during a FWI. In order to assess thermal energy losses, CARS thermometry has been found to be an accurate, non-intrusive temperature measuring technique which can be used for in situ probing of combustion processes. Due to increasing power densities of newly developed combustion engines as well as continuously increasing aerial traffic, the adverse effects of FWI on combustion affect the efficiency and environmental impact of aircraft engines only increases. By curbing the losses induced by maintaining combustion in a confined space, depleting fuel reserves are better conserved and adverse environmental effects curbed.

This study focuses on the evaluation of temperature data obtained by broadband RCARS thermometry of a turbulent FWI as well as the delay of the probe pulse with respect to the pump/Stokes beams. Since the dephasing of the excited rotational states is not constant across the rotational states, the measured relative population of each state changes with increasing delay. In order to compensate for the resulting spectral heating issue, the pulse delay needs to be accounted for when generating the spectral libraries used to obtain temperature information from the spectral data captured by the camera. The integrity of these spectral libraries has been investigated by performing a spectral fitting routine of ideal CARS spectra computed by a Matlab code. The spectral libraries consist of Nitrogen CARS spectra ranging from 200K to 2400K in steps of 100K. The probe pulse delays investigated range from 50 ps to 450 ps. The temperature error measured in this study reduces with an increase in temperature and alternates between overestimating and underestimating the actual temperature of the investigated spectrum.

Keywords: CARS thermometry, FWI, turbulent combustion

ACKNOWLEDGEMENTS

With this thesis, my years at this university are coming to an end. I was able to learn a lot about engineering, but also about others and myself thanks to the continuous support of the people around me.

Firstly, I would like to thank Dr. Alexis Bohlin, who not only supervised my thesis but spent many hours with me and other students discussing and evaluating the research we have done. His insights, advice and patience helped me a great deal in finalising this thesis and dealing with the struggles that came with it. His passion for his research has been inspiring and made me appreciate a field of research with which I had no contact before. I'd also like to thank Dr. Chris Kliewer at Sandia National Laboratories and Prof. Andreas Dreizler at TU Darmstadt for allowing me to use and providing me with their research data on turbulent Flame Wall Interactions.

I would like to thank my thesis committee, Dr. Arvind Gangoli Rao, Dr. Roger Groves and Dr. Dmitrii Kliukin for taking the time to evaluate me and my work. I realise being on a thesis committee adds quite some work to a busy schedule and appreciate their willingness to do so for me.

I would like to thank TU Delft and all the professors, lecturers, supervisors, teaching assistants and peers who guided me on my way to becoming an engineer. I couldn't possibly list all the things I have learned in these past years and every one of them has contributed to me reaching my goal.

I would like to thank my friends who accompanied me on my journey and made life here in Delft some of the best years I had. I'd like to thank Simon Baar, who has not only been available for advice whenever I needed but to this day, is a role model to me. I thank Benedict Bartels, whom I did all the studying and all the assignments for our courses with. He made a stressful and at times frustrating period of my life much more enjoyable and helped me remain healthy throughout. I thank Jan Sieksmeyer who, despite being so far away, is one of the most loyal friends I have and whos insights have helped me see some important things much more clearly.

Finally, I would like to thank my family. All my life I could always rely on their support. They taught me the value of education and provided me with everything I needed to chase what I wanted the most. I could not have done this without them.

Karim El Sioufy
Delft University of Technology
25th of March, 2020

1

INTRODUCTION

This master thesis will provide a detailed overview of the background knowledge required for understanding a coherent anti-Stokes Raman scattering (CARS) thermometry experiment for the investigation of Flame-Wall Interaction (FWI) as well as the results of one such experiment conducted at Sandia National Laboratories. Additionally, a study has been conducted to investigate the effect of probe pulse delays on the accuracy of the technique.

Combustion is an exothermic reaction between a fuel (or reactant) and an oxidant. The thermal energy released through this process, commonly at temperatures up to several thousand degrees Celsius, is one of the most essential drivers of modern machinery, especially in the transport sector and the generation of electrical energy [1]. In most applications, this process is controlled within a combustion chamber, allowing the controlled channelling of both pressure and temperature in order to create thrust or electricity for instance. While modelling of free flames has come a long way, confined flames are still insufficiently researched and can only be predicted using incomplete models or approximations. It has been shown that the interaction between a combustion process and the physical boundaries of a combustion chamber cause incomplete combustion, temperature fluctuations and exhaust gas composition changes. This ultimately affect both the efficiency and the environmental impact of the combustion process. Additionally, fuels with a relatively high laminar flame speed such as hydrogen [2] become prone to phenomena such as flashback [3][4], which may lead to severe accidents.

Several challenges arise when researching combustion processes. One of the most important parameters in a combustion process is temperature. It is a direct indicator of how much energy has been released and strongly influences the composition of the exhaust product. Its accurate measuring is essential to combustion research. Since combustion phenomena can occur on very small scales and occur in harsh high-temperature environments, non- or minimally invasive measurement methods such as certain laser diagnostics (i.e. CARS, LIF) have proven their superiority in terms of precision and accuracy [1].

Through the research of FWI, the combustion processes essential to modern industry and transport can be better understood and modelled. Adapting combustion chamber designs to wall-induced losses may lead to an increase in fuel efficiency. This will not only buy us some time to solve the problem with the depletion of natural resources such as gas and oil, but also decrease the continuous costs of running combustion machinery (mainly fuel costs). In addition, better control over the exhaust products, which are temperature dependant, provides an additional way to mitigate the most harmful ones. While none of the exhaust gases are "good" for the environment, some have a more direct/severe impact on human health and the atmosphere than others. A direct consequence of incomplete combustion is the emission of unburned hydro-carbons (UHCs) as well as carbon monoxide (CO) molecules which have not been oxidized due to either a lack of oxygen in the combustion chamber or a loss of temperature that inhibits further temperature driven chemical reactions. The presence of a wall has been shown to contribute to an increase of these particles. Unlike carbon dioxide, carbon monoxide is highly poisonous to humans and can damage the ozone layer by breaking up Ozone (O_3) molecules in order to oxidise, as visualised in Equation 1.1. [5]

$$O_3 + CO \rightarrow CO_2 + O_2 \tag{1.1}$$

Commercial aircraft fly at an altitude of about 10km which is where the ozone layer starts. This means that most of the CO produced immediately comes into direct contact with the ozone layer. Even though the emission of greenhouse gases cannot be avoided using modern combustion technology, improved combustion control can allow the designer of a combustion engine to influence which one is primarily produced. Eventually, once hydrogen combustion has been developed to a point that it can be safely and universally implemented, water vapour alongside a so far undetermined amount of NO_x could become the only emission of combustion technology. For that to happen, aspects such as losses and flame stability in combustion chambers need to be modelled more accurately first.

CARS is a spectroscopy technique which has been developed to induce strong, laser like signals containing information on the rotational and vibrational energy states present in the probe volume. By interpreting the population distribution of the rotational energy states using the Boltzmann distribution, accurate temperature data can be obtained from the probe volume. The use of high powered lasers makes CARS a robust thermometry technique with the potential to advance combustion research. This thesis aims to highlight the advantages of CARS as a thermometry technique and explores the accuracy and precision of the technique as it is used today. The technique has been improved to probe a wide range of energy states within one snapshot and, instead of point measurements, measure a 1-dimensional (line) probe volume. This has greatly improved the utility of the technique for combustion application, however now potential error sources have been introduced as well. The cameras which capture the generated spectra is limited by it's dynamic range. In order to record an accurate spectrum, both the least and the most intense signals need to be captured accurately with respect to one another. Their relative intensity is what allows for the reading of temperatures from spectral data. A way this can be compensated for is by delaying the probe laser which follows the initial excitation of the probe volume. By doing so, the range of signal intensities captured by the camera is decreased to fit within its dynamic range, allowing for the simultaneous capture of spectral data from both hot and cold areas. An experiment has been conducted to investigate if and how this delay affects temperature measurements, using Matlab scripts written to generate spectral libraries and interpret experimental CARS spectra as temperature by performing a spectral fitting routine.

Firstly, Chapter 2 provides an introduction into combustion theory as well as clarification for commonly used terminology. In Chapter 3, laser diagnostics are elaborated with a detailed focus on CARS spectroscopy and how to use CARS spectra to obtain temperature information. Chapter 4 presents the issue of Flame-Wall Interaction and how it can be experimentally assessed. Additionally, a review of a number of studies on FWI using a variety of measurement techniques is provided. In Chapter 5, a FWI research project using an advanced CARS technique which aims to assess the effects of turbulence is elaborated. The Matlab code used to process and evaluate the resulting data is also presented as it becomes the foundation of the investigation conducted for this thesis. This investigation and its results are presented in Chapter 6. Lastly, conclusions and recommendations for further research are presented in Chapter 7.

2

COMBUSTION FOR POWER GENERATION AND PROPULSION

This chapter will clarify some of the terminology and underlying principles of the matter described in the following chapters. Due to the temperature measurements of combustion lying at the heart of the upcoming thesis, the concepts of combustion and temperature as well as the msot commonly used terminology in combustion research are presented in Section 2.1. Subsequently, the issue of emissions due to (hydrocarbon) combustion is elaborated in section 2.2. Lastly, some terminology is clarified in Section 2.4 which is used to describe the performance of an experiment.

2.1. THE PROCESS OF COMBUSTION

Combustion is a high-temperature, exothermic redox chemical reaction between two reactants, a fuel and an oxidant. Exothermic means that the process generates heat (rather than consuming heat) and redox is short for reduction-oxidation reaction. Aside from the release of thermal energy, a variety of exhaust gases are produced, commonly named the combustion products. These products and their respective mass fractions depend on the fuel that has been used. The main fuel type in modern combustion technology is called hydrocarbon. This refers to substances such as methane or kerosene which consist entirely of hydrogen and carbon atoms, excluding naturally occuring impurities.

2.1.1. STOICHIOMETRY

In an ideal, stoichiometric combustion process all the available fuel reacts with all the available oxygen. Stoichiometry refers to the optimal mixing ratio between oxidant (for example air) and fuel, under which the maximum amount of heat is released [6]. The mixing ratio of fuel and oxidant is calculated according to eqn. 2.1

$$\phi = \frac{\left(\frac{m_{fuel}}{m_{oxidizer}}\right)_{actual}}{\left(\frac{m_{fuel}}{m_{oxidizer}}\right)_{stoichiometric}} \tag{2.1}$$

Here, m refers to the respective mass or the number of moles, which can both be used to compute this ratio. A fuel rich mixture results in $\phi > 1$, a fuel lean mixture results in $\phi < 1$ and a stoichiometric mixture is achieved when $\phi = 1$. In order to compute this ratio, the mass ratio at which stoichiometry can be achieved for a given fuel and oxidizer is required.

The chemical equation for the stoichiometric combustion of hydrocarbons can be found in eqn. 2.2

$$C_aH_b + c \cdot O_2 \rightarrow a \cdot CO_2 + \frac{b}{2} H_2O \tag{2.2}$$

with

$$c = a + \frac{b}{4} \tag{2.3}$$

Here, C_aH_b denotes a hydrocarbon consisting of an 'a' amount of carbon atoms and a 'b' amount hydrogen atoms and cO_2 denotes a 'c' amount of oxygen molecules, which subsequently turn into a fixed amount of carbon dioxide and water vapour depending on the fuel composition. Solving this equation for c, provided that the fuel (and thus a and b) is known, the exact amount of oxygen molecules per fuel molecule for stoichiometric combustion can be computed. For example, one molecule of methane, or C_1H_4, would require two Oxygen molecules for a complete combustion. Hence, a combustion process where 2 oxygen molecules for each available methane molecule is considered stoichiometric. From this, the mass ratio of fuel to oxygen can be easily derived using the well documented masses of all atoms involved. When using air as an oxidizer, the mass of the air that contains the required amount of oxygen needs to be used to compute the mass fractions instead.

However, this is only the case in an ideal combustion process. In a real combustion process, maximum adiabatic flame temperatures are achieved with a slightly fuel rich mixture. The equivalence ratio for which heat release is maximised varies for each fuel.

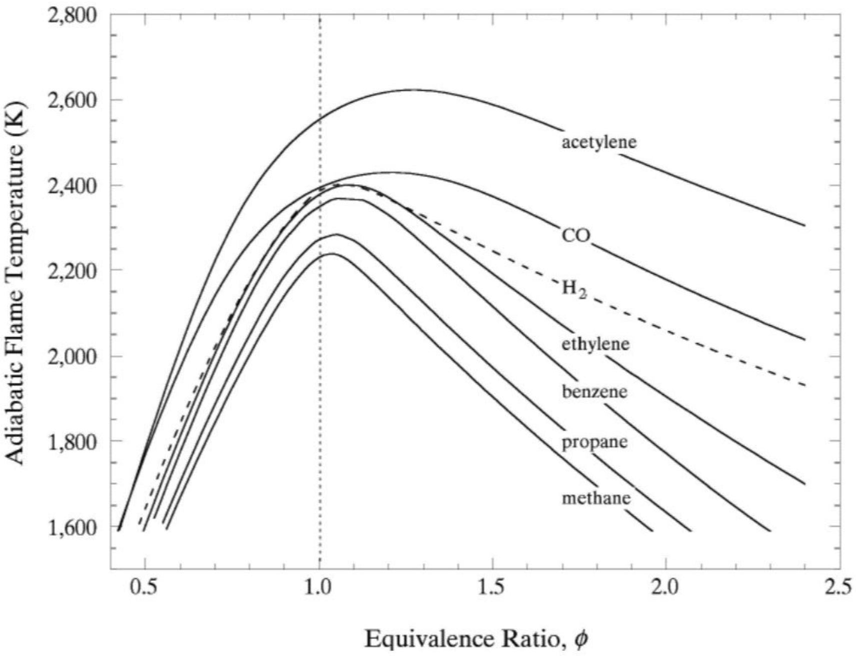

Figure 2.1: Adiabatic flame temperature vs equivalence ratio for varying fuels. All fuels have their maximum adiabatic flame temperature at slightly fuel rich conditions but each at their own equivalence ratio. [7]

In Fig 2.1 the dependency of the adiabatic flame temperature with respect to equivalence ratio and fuel type is shown. The maximum adiabatic flame temperature of these fuels occurs at fuel rich conditions, meaning that there is "too much" fuel available in the combustion process with respect to the available oxygen. However, the equivalence ratio at which this maximum can be encountered varies for every fuel type. This implies that in order to optimise a combustion engine, the type of fuel that is going to be used needs to be taken into account as not only the possible maximum heat release varies but also the mixing ratios at which they occur. This has a direct impact on the exhaust products produced as well.

2.1.2. FLAME STRUCTURE

In general, a flame can be described by separating it into 3 distinct zones: the preheat zone, the reaction zone and the equilibrium zone, where the reaction zone can be further split into the inner layer containing the actual flame and the oxidation layer.

In Fig. 2.2 a temperature profile for a standard combustion process is shown. The fuel starts out too cold to react and is heated by the ongoing combustion process until it reaches it's combustion temperature. The flame location where this process occurs is called the pre-heat zone. At the combustion temperature,

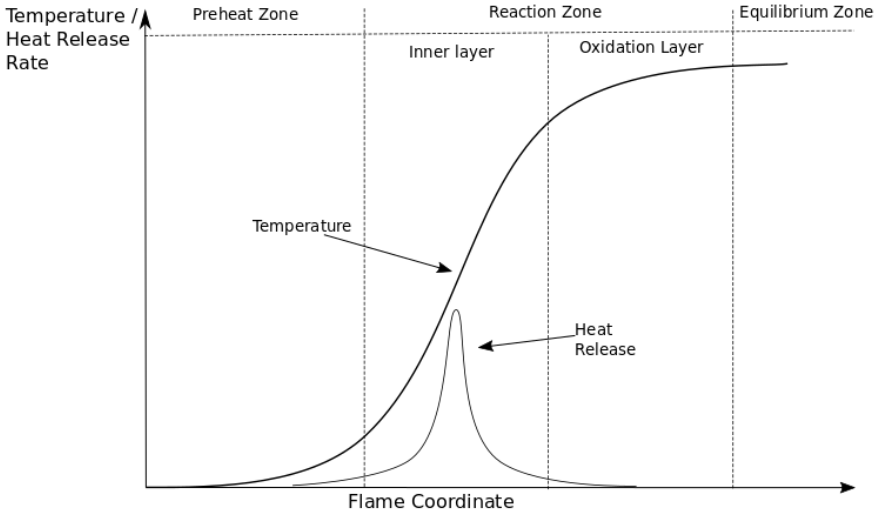

Figure 2.2: Temperature profile of a flame with indicated flame zones and heat release. Ther fuel is heated by the ongoing combustion process in the preheat zone until it reaches its combustion temeprature. After the initial peak heat release, the oxidation of unreacted radicals continues to produce heat until the equlibrium point is reached and the reaction ends.

the molecular bonds no longer hold, the fuel molecule breaks apart and bonds with the available oxygen in the reaction zone, releasing heat. This is referred to as the reaction zone, which can be further split into the inner and outer layer. The inner layer contains the flame front a major portion of the total heat release. The inner layer is also referred as the oxidation zone, where remaining OH and CO radicals further oxidise into H_2O and CO_2, respectively. Once the final temperature is reached and no further oxidation occurs, the equilibrium zone is reached. This means that the combustion process has been completed, resulting in a specific composition of exhaust gases at a certain temperature, also referred to as emissions.

The position of the flame front can be detected using a variety of methods. Hoferichter [8] stated the flame front to be the boundary between bright and dark regions. A more precise measurement can be done by making use of radical chemiluminescence. For instance, the intermediate species OH (hydroxide), which is formed in the flame front, emits a characteristic electromagnetic signal (in the UV region) if it has been electronically excited (OH^*). This radiation can be captured with a camera and serves as an indicator for the flame front position in a variety of FWI research projects [9],[8],[10],[11][12]. Additionally, flame front detections can be done using Mie scattering images from the tracer particles of ($\mu-$)PIV measurements. Along with the density of the mixture, the density of particles at the flames front changes drastically due to gas thermal expansion. The sudden change in signal intensity can be interpreted as the flame front location [13],[12][14].

2.1.3. QUENCHING POINT

Another flame parameter important to FWI research is the quenching point. Generally speaking, the quenching of the flame means that not enough heat is available to sustain the combustion process any longer. In other words, the flame is extinguished due to a lack of activation energy for the remaining fuel. Together with the first point of contact between wall and flame, this flame dependant location can be used to determine the quenching distance, which can be used to compare to a free burning flame and thus quantifying the quenching effect of a wall on a flame. Just like the flame front, there exists no generally applicable definition of this point and researchers are usually left to find a valid approximation for it themselves. Jainski et al. [12] have defined the quenching point to be the location where the OH-gradient falls below 0.5, which is an assumption that has been used in DNS studies as well [15].

2.2. EMISSIONS

The remains of fuel and oxidant left behind after a combustion process are called the combustion products. Especially in the transport sector, they are more commonly referred to emissions. The type of emissions produced in a combustion process as well as their quantity vary depending on the fuel, the oxidant, the mixing ratio and the combustion temperature.

The only two products of a complete, stoichimetric combustion process using hydrocarbons would be water vapour (H_2O) and carbon dioxide (CO_2)[16]. However since this assumes ideal, complete combustion, this is not achievable in a modern combustion engine.

Firstly, not all of the carbon atoms completely oxidise into CO_2. If, for example, a fuel/oxidiser mixture is too fuel rich, soot and carbon monoxide (CO) are produced instead. While soot is immediately noticeable, both visually and when breathing it in. CO on the other hand has no smell, no taste, no colour and can therefore be breathed in without noticing. While it is not one of the greenhouse gases, which are the primary focus of modern environmental efforts, it is dangerous nonetheless because it oxidises slowly (which means it remains in the atmosphere) and can be lethal at high concentrations.

Due to the fact that most combustion engines use air as an oxidiser, the presence of nitrogen (N) in the combustion chamber leads to the production of nitrogen-oxides (NO_x). Nitrix oxide (NO) in the atmosphere is one of the leading causes for acid rain whereas nitrogen dioxide (NO_2) is a greenhouse gas. Unlike most emissions, the production of NO_x does not depend on the fuel but is mainly a by product of using air as an oxidiser. It's production is highly temperature dependant.

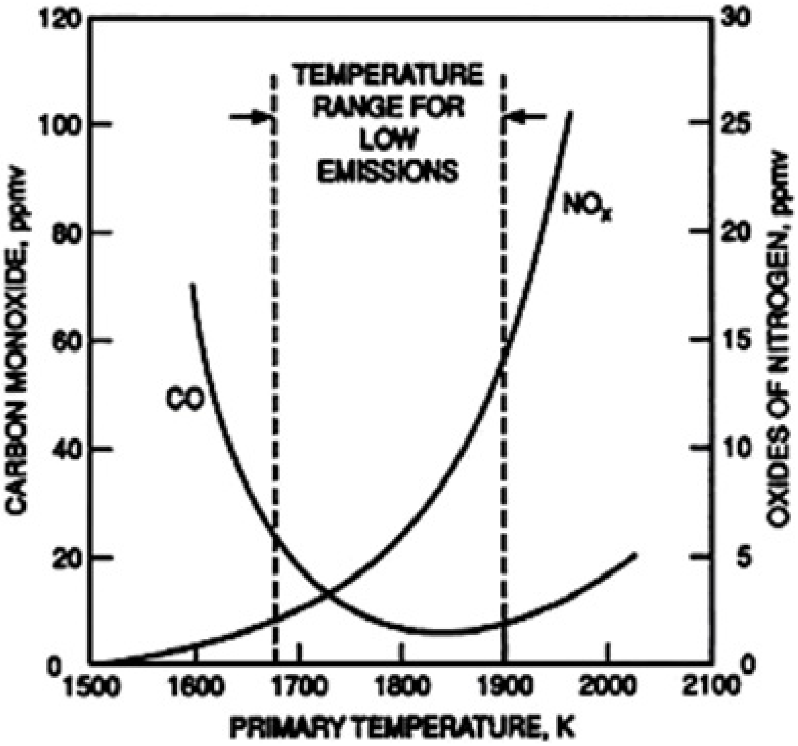

Figure 2.3: Temperature dependence of CO and NO_x formation in a hydrocarbon combustion process. Vertical dotten lines mark the temperature range of minimum emission. Emission concentrations are given in ppmv on the y-axis, combustion temperature is given in K on the x-axis. [17]

In Fig. 2.3, a comparison between CO and NO_x production is shown with respect to the temperature of the combustion process. The two vertical dotted lines enclose the temperature range at which the total emission of both of these byproducts is minimised. While N requires high temperatures to oxidise, CO is one of the main components produced when a hydrocarbon is used for combustion. Due to their inverted temperature behaviour, it is clear that all emissions cannot be minimised at the same time in a hydrocarbon fuelled combustion engine. Minimising the emission of one species will lead to an increase in the other. The highlighted center region is the range of temperatures at which the sum of both emission components can be minimised.

In addition to the two main combustion products, a variety of pollutants may be emitted, including nitrogen oxides (NO_x), carbon monoxide (CO), unburned hydrocarbons (UHCs), sulfur oxides (SO_x) and particulates such as Soot (C) [18]. NO_x is a pollutant commonly produced by air-breathing combustion engines, which use the ambient air as an oxidant. If the temperature of the combustion process is sufficiently high, some of the available oxygen will react with the N_2 molecules instead of the fuel. CO is a radical, which is a general term in chemistry for an atom or molecule which has unpaired valence electrons, which makes them highly reactive. Unburned hydrocarbons are small droplets of fuel that have not undergone combustion. Sulfur oxides are a byproduct of most combustion processes which rely on fossil fuels [19]. The sulfur is an impurity within the fuel and oxidises along with the other combustion components due to the high temperatures. Lastly, particulates such as soot are produced, especially during fuel rich combustion processes [6]. The concentration of these products within the exhaust depends not only on the mixing ratio but also on the temperature in the combustion chamber, as can be seen in Fig. 2.3.

This graph shows the trend of CO and NO_x formation with respect to temperature in the combustion process of carbohydrates. While CO production is maximised at relatively low temperatures ($\approx 1600K$), which could be a symptom of incomplete combustion, NO_x production exponentially increases with temperature. This highlights the importance of temperature control within a combustion chamber, as it has a direct relation to the pollutants that are produced in the process. Ideally, the engine should be operated within the temperature range for low emissions, which is indicated which the dotted vertical lines.

2.3. THERMOMETRY IN EXPERIMENTATION

Thermometry is the measurement of temperature. Due to the fact that temperature is one of the main defining parameters of a combustion process, accurate thermometry is a vital part of combustion research. Throughout history, many different ways of measuring temperature have been developed, most of which have some unique applications, making them favourable in certain temperature ranges or with respect to an object/circumstance.

Commonly employed temperature measurement techniques include devices such as thermocouples or infra-red cameras. While an infra-red camera simply captures all electromagnetic waves within a certain spectrum (700nm-1mm wavelength) and interprets those based on the well established relationship between temperature and wavelength within the thermal infrared spectrum, thermocouples interpret temperature dependant voltage variations within a material. While these techniques are usually useful in their own ways, they are basically not suitable for the type of combustion research which this literature study builds up to. Infrared cameras for example are primarily suited to observe surfaces such as metal plates. They are incapable of distinguishing multiple heat sources in it's line of sight, making them basically unusable for high accuracy 3 dimensional applications such as flame investigations. Additionally, the temperature ranges that can be observed with such cameras are often limited and not as accurate within the required range as other methods. Thermocouples are not only invasive, hence would distort a FWI with it's mere presence, but could also only be used to measure the temperature of the wall to which they are attached.

In the past few decades, laser diagnostics have become a reliable measuring technique for precise, local temperature measurements and are especially suited for combustion research due to being non-intrusive, unlike a thermocouple for instance [1]. CARS thermometry is one of these methods and is explained in detail in Chapter 3 due to its importance to the upcoming thesis work.

2.4. EXPERIMENTATION TERMINOLOGY

This section clarifies 4 important parameters which describe the performance of an experimental setup. Those terms are robustness, sensitivity, precision and accuracy. Note that the definition of these parameters may vary depending on the experiment/the specific context in which they are used. Examples made in this section will relate to how they may be used in the context of an FWI experiment.

Robustness is generally defined as the quality or condition of being strong and in a good condition or the ability to withstand or overcome adverse conditions or rigorous testing. In experimentation, increasing the robustness of a design means finding the settings and/or methods which minimise the influence of external and uncontrollable influences that could distort the results. This is especially important when looking at small scale phenomena with minimal changes, where slight inaccuracies could already lead to misconceptions.

Sensitivity, or responsiveness, is a measure that relates the change of one parameter to a change in your experimental results. For example, a sensitivity analysis is performed by slightly altering design relevant parameters one by one, usually by a relatively small amount, and observing how it changes the overall result. Finding out that a small change in a certain parameter has a grave effect on the end result indicates that this parameter needs to be monitored and regulated carefully in order to acquire accurate results.

Precision and Accuracy are best explained together, using visuals such as Figure 2.4.

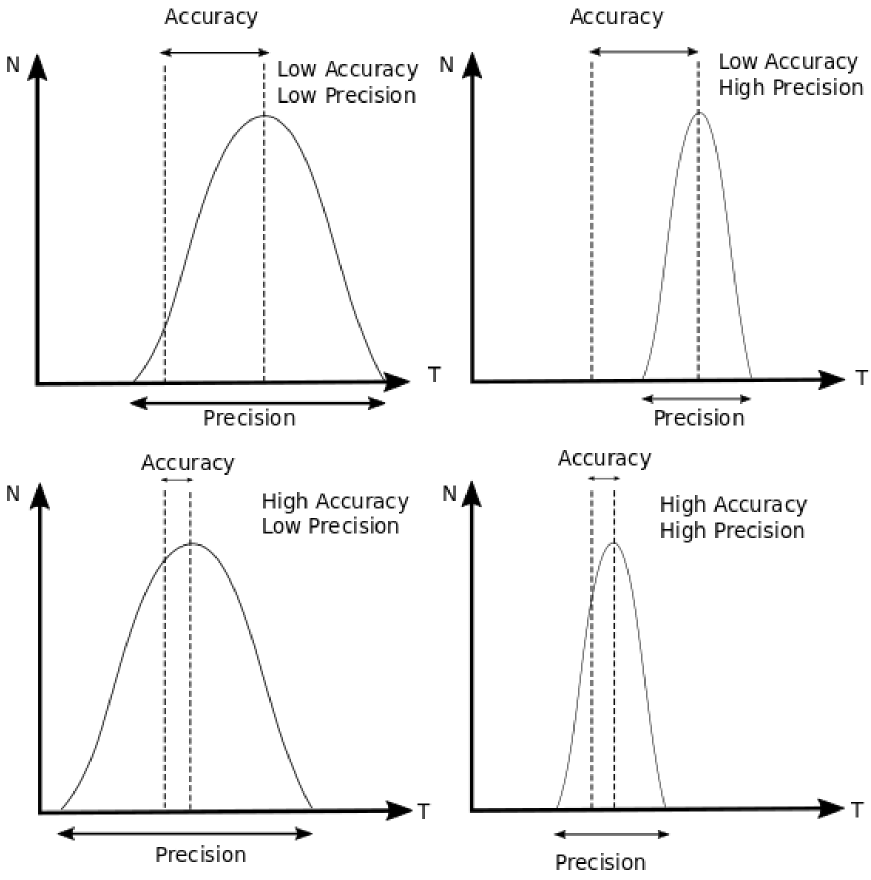

Figure 2.4: Example of how accuracy and precision apply in a thermometry experiment. N is the number of measurements, T the temperature obtained. A high accuracy means the average temperature measured in all measurements is close to the real temperature, high precision means a low deviation of each measurement from the average temperature obtained.

In this example, the difference between precision and accuracy is visualised using a hypothetical experiment which takes multiple temperature measurements of a flame. Due to experimental imperfections and data evaluation inaccuracies, not every measurement might yield the exact temperature as the actual flame temperature or as the temperature measured in a previous attempt. When conducting an experiment that consists of a series of measurements, as is very common in combustion research, precision and accuracy describe the 2 main ways in which the measured data relates to the reality one is trying to observe. A measurement series with high precision (top right) will yield a small data spread, meaning none of the measurements differ too significantly from each other. This means that results using said technique are very well reproducible, but might still be faulty due to a common offset. Accuracy determines how much the average value of the measured results deviates from reality. Hence, a highly accurate measurement series (bottom left) might contain a lot of deviations between singular measurement points, however the dataset as a whole (i.e. an average value) can yield results close to the actual value. Due to the Boltzmann distribution (explained in detail in Chapter 3) having a very similar shape to the curves above, these concepts translate well to the analysis of the experimental data to be evaluated in the upcoming thesis. To give a more specific example, one could measure the surface temperature of a metal plate which is at 300K using 5 consecutive measurements.

A measurement purely optimised for precision might yield a dataset like this:

$$a = \langle 310.1, 309.9, 310.0, 310.2, 309.8 \rangle \tag{2.4}$$

whereas an experiment purely optimised for accuracy would results in a dataset like this:

$$b = \langle 298.3, 305.6, 303.4, 295.7, 297 \rangle \tag{2.5}$$

In order to use the first dataset, one would require the information that each measurement is offset by about +10K from the actual wall temperature. In order to use the second measurement series one would need to make sure that enough measurements are taken so that the average of the dataset results in 300K. Ideally one strives to achieve both maximum accuracy and maximum precision if possible.

3

BURNER EXPERIMENTS AND LASER DIAGNOSTICS

The investigation of combustion processes comes with a variety of challenges and requirements which need to be accounted for when designing the experiment. Additionally, when investigating FWI, the presence of a wall which, among other perturbing effects, reduces the optical access to the probe volume, only increases the challange of obtaining accurate temperature data. This chapter will first elaborate upon some of the requirements which a FWI experiment design needs to account for. Subsequently, CARS thermometry is presented as a technique which fulfils these requirements and a comprehensive summary of how this technique is employed is provided.

3.1. EXPERIMENTATION REQUIREMENTS

Once a clear research goal has been defined, an experiment needs to be designed with well controlled boundary conditions to ensure that any of the measurements are taken only from the subject of interest. For this thesis, this point of interest is the temperature profile of the FWI region, specifically the flame front and the quenching point. In order to obtain conclusive results from the measurements, the flame parameters need to be controlled as precisely as possible. The first of these parameters is the mixing ratio, which is primarily determined through mass flow controllers and mixing enhancing burner components. Thorough mixing of fuel and oxidant are necessary to ensure a steady FWI when investigating SWQ. To prevent mixing with the stationary, ambient air, coflows of gases which have a relatively small influence on the combustion process such as nitrogen can be employed. Flame structure and shape need to be considered as well. All experimental setup parameters relating to the burner will be discussed in detail in chapter 4.

An experiment investigating flames with high accuracy will benefit from using non-intrusive, in-situ probing methods. Non intrusive means that no physical probe is present in the flame (i.e. thermocouples) which could distort the flow or inhibit complete combustion. Due to one of the main issues with FWI being incomplete combustion and temperature loss, any additional loss added by the measurement tools themselves would decrease the experimental accuracy. In situ probing means that measurements are taken directly at the location of interest at the time of the combustion process. The alternative to this would be an interpretation of the combustion process based on the temperature and molecular composition of the exhaust gases.

Lastly, a requirement for the temporal and spatial resolution of the probed data has to be formulated. Flow phenomena in flames can occur on a very small scale, especially when investigating turbulent combustion processes. Additionally, the high velocity with which most flames burn makes it difficult to obtain a stationary image. Due to the fast changing nature of the flame, an experiment with low temporal resolution will only be capable of measuring an average state of the flame.

In recent years, optical measurement techniques using lasers have established themselves to be among the most robust and accurate tools for investigating flow fields, species concentrations and temperature of

FWIs. The phenomena to be observed occur within a relatively short time and especially in turbulent flames, local combustion characteristics such as temperature change rapidly. This raises a need for a large number of instantaneous measurements (snapshots). Fast measuring prevents temporal averaging and gives more accurate data on the current flame state. With a large amount of these measurements over time, trends and limits can be determined. Optical measurement techniques have been developed to deal with these challenges. Among them, Coherent anti-Stokes Raman scattering (CARS) spectroscopy has proven itself as robust and precise measuring technique for both species detection and thermometry. The ultrafast broadband rotational CARS technique was used to obtain the experimental results which will serve as the basis of the upcoming master thesis.

3.2. THE ENERGY LEVELS OF A MOLECULE

This section will elaborate upon the quantum-mechanical representation of molecule energies. The knowledge established here will be used in the next section to explain the various ways in which light can be scattered and how a CARS signal is generated.

A quantum mechanical system or particle that is bound can only take on certain discrete values of energy called energy levels. In total there are three types of discrete energy states, electronical, vibrational and rotational. Translational energy, which can technically be considered a fourth type of energy state, is considered continuous and can therefore be described by classical/continuum mechanics [20].

In Fig. 3.1 the definition of vibrational and rotational motion of a molecule is shown. The main contribution of an atoms weight comes from their nucleus. Due to the small size of the nucleus (femtometers), the atoms can be modelled as point masses connected by a bond. For vibrational motion (upper), this bond is modelled as a spring, for rotational motion (lower) it is modelled as a stiff rod. These 2 models are referred to as the harmonic oscillator and the rigid rotator, respectively.

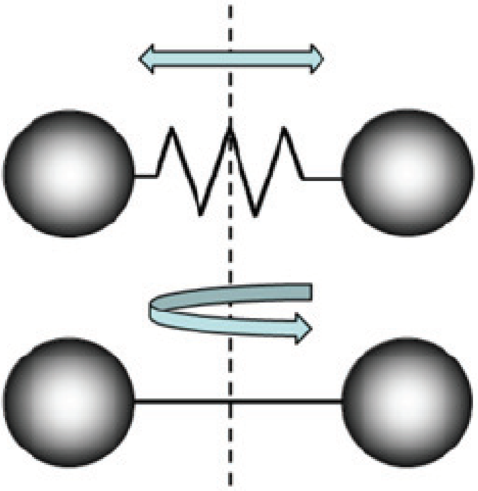

Figure 3.1: Model of a diatomic molecule. Harmonic Oscillator (upper) and rigid rotator (lower) [21].

Note that mono-atomic molecules are considered to contain no vibrational or rotational energy. The former is based on the fact that at least 2 atoms need to be bonded so the bond can act as spring and allow the molecule to vibrate. The latter is based on the negligible mass of a single molecule as well as the femtometer radius of the nucleus, which is the main contributor to a molecules mass, resulting in a mass moment of inertia which is just as negligible. While a diatomic molecule doesn't have a lot of mass, the fact that the center of mass lies between the two nuclei significantly increases the moment arm, making the mass moment of inertia non-negligible. Only particles that are bound are described with discrete energy levels. A visual representation of the molecular energy model can be found in Fig. 3.2.

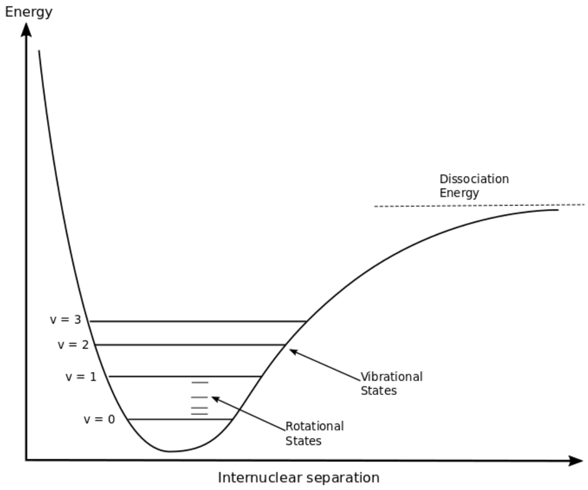

Figure 3.2: The anharmonic oscillator model, showing energy states of a diatomic molecule. The curve represent the average internuclear distance of the atoms with respect to energy. Lines marked with a v are vibrational quantum numbers, an example for rotational energy levels is shown above the v=0 level.

Here, the average internuclear distance between 2 atoms bound in a molecule are shown in relation to the total energy of the molecule. Both rotational and vibrational energy levels are indicated as well as the wavelengths corresponding to the energy required to cause a transition.

There are several things to be observed from this model. Firstly, the left side of the curve behaves almost like a parabola, converging towards a minimum distance. The atoms of a molecule need to have a certain minimum distance from each other in order to maintain their structure. Forcing two atoms closer to one another can eventually lead to nuclear fusion and change the molecule fundamentally. Secondly, while the most simple version of the model describes the internuclear separation as a parabola, in reality the maximum internuclear distance (right side of the curve) increases exponentially until the so called dissociation energy is reached. The dissociation energy is the amount of energy required to break the bonds between the molecules' atoms due to the forces resulting from strong vibrational and rotational motion exceeding the bond strength. The first step of hydrocarbons combustion depends on this effect. Bigger molecules such as methane are heated by an external source such as an ongoing combustion process, which causes them to reach their dissociation energy and break up into smaller molecules. Those molecules, called radicals, can then continue to sustain the combustion process, release more thermal energy and repeat the process for the rest of the unreacted fuel.

Increasing the energy contained in a molecule can only be done discretely. The highest energy shifts a molecule can experience are on the electronical level. However, CARS does not probe electrical energy levels so this will not be further elaborated upon here. Within each electronical level, a range of vibrational states exists. Just like the electronic levels, there is a ground state from which a molecule can be excited. The harmonic oscillator model shows these levels to be equidistant, assuming that the same amount of energy is required to excite a molecule on any vibrational level to the next one. However in reality, the energy required decreases with increasing vibrational energy level and energy level transitions of multiple levels at once has been observed. This causes the highest levels to nearly form a continuum just before the dissociation energy is reached. This is shown in equ. 3.1, which can be used to calculate the energy of vibrational states.

$$E_v = \hbar\omega_{vib}\left(v+\frac{1}{2}\right) - \hbar\omega_{vib}x_e\left(v+\frac{1}{2}\right)^2 + \ldots \tag{3.1}$$

where $\hbar$ is the reduced Planck constant, ω_{vib} the vibrational frequency, x_e the anharmonicity constant and v the vibrational energy level. Due to the negative contribution of the v^2 component, the energy required for a vibrational energy level transition decreases as the vibrational energy of the molecule increases.
On each vibrational level, a range of rotational energy levels exist. Unlike vibrational energy, an almost

quadratically increasing amount of energy is required to reach higher rotational levels. This is shown in equ. 3.2 which describes the eigenenergies of the rigid rotator.

$$\epsilon_J = BJ(J+1) - DJ^2(J+1)^2 + ..., \quad D = \frac{4B^3}{\omega_{vib}} \tag{3.2}$$

where J is the rotational energy level, B the rotational constant and D the centrifugal constant. Note that there are more correction terms to be added to both equ. 3.1 and equ. 3.2, further improving their accuracy, however they were omitted here as it exceeds the scope of this study.

Despite occurring on different scales, these different types of energy are usually coupled. An increase in vibrational energy will cause an increase in the average internuclear distance, increasing the average moment of inertia of the molecule and thus affecting its rotational motion as well. The most commonly encountered couplings are called as follows: a simultaneous shift in vibrational and rotational energy is referred to as a rovibrational energy shift, a shift in electrical and vibrational energy is called vibronic and and simultaneous shift in all 3 of the above is called a rovibronic energy shift.

3.3. SCATTERING

The scattering of light is the essence of CARS spectroscopy. A photon that collides with a molecule will be scattered off of it, changing it's direction and, possibly, it's wavelength. There are 2 types of scattering, elastic or Rayleigh scattering and inelastic or Raman scattering. Rayleigh scattering describes a photon which contains the same amount of energy before and after colliding with a molecule. Raman scattering can occur in two different ways, either the molecule absorbs some of the photons energy (Stokes) or it loses energy to the photon (anti-Stokes). The magnitude of the change in energy corresponds to a shift in the molecular energy levels and is called Raman shift. The process is illustrated by Fig. 3.3.

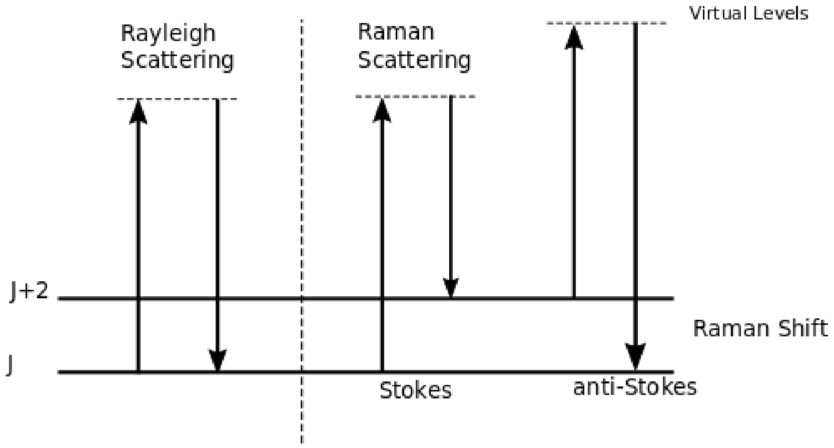

Figure 3.3: The 3 types of scattering. From left to right: Elastic/Rayleigh scattering which is the emission of a photon with the same wavelength as the absorbed photon. Stokes-Raman scattering causes the emitted photon to have less energy than the incident photon. Lastly, anti-Stokes-Raman scattering causing the emitted photon to have a higher energy than the incident photon.

The bottom line represents the original (ground) state of the molecule before interacting with a photon, the arrows represent the sudden energy increase due to the presence of a photon and the dashed lines represent the resulting virtual energy state. From left to right, the molecular energy changes are sketched for Rayleigh scattering, Stokes Raman scattering and anti-Stokes Raman scattering. In the case of Raman scattering, the molecule is left at a different eigenstate than the one previous to the interaction, which is represented by the second continuous line. Unlike these eigenstates, a virtual energy level is not an actual state in which the molecule can exist. During the time of interaction between the molecule and the photon, they can be considered a system with a total energy equal to the sum of their respective contributions. As soon as the photon ’leaves’ the system, the molecule assumes an eigenstate again.

3.4. CARS SPECTROSCOPY

In order to create a CARS signal, 3 lasers beams need to interact with the medium to be investigated: the pump, the Stokes and the probe beam. The pump beam and the Stokes beam excite the molecule to an elevated rotational or vibrational energy state. The energy difference between the two laser beams needs to exactly match the transition energy required to cause a discrete shift in energy for the molecule. Both lasers need to be focused on the same same location at the same time in order to cause this effect and the excitation will only be temporary. A probe beam can now be scattered of the rotationally or vibrationally excited molecule. This will cause the photons of the probe beam to absorb the excess energy of the molecule, which can be observed as a so called Raman shift in the resulting frequency spectrum. The shifted wavelength of the probe laser provides information on the energy level transition previously induced.

Due to the elevated energy levels of the incident molecules, the probe laser’s photons have a slightly shorter wavelength after being scattered. This gives the resulting CARS signal beam a slight shift towards the blue wavelength range of the electromagnetic wave spectrum. This resulting signal beam is then relay imagined through a low pass filter into a spectrometer, where the signal is decomposed with respect to the wavelengths present in the beam.

There are two different types of CARS, vibrational and rotational. This refers to the type of energy level that is being elevated through excitation. While both concepts work similarly, they can be used in a complementary fashion due to the fact that they excel at different temperature ranges. Vibrational CARS is especially suited for temperatures at/beyond the upper limit of the optimal rotational CARS temperature range. This stems in part from the fact that there are a lot less observable vibrational energy levels. Consequently, vibrational CARS is a lot less sensitive at low temperatures and can therefore not yield results that can compare to rotational CARS in terms of accuracy. Additionally, the intensity of the rotational CARS signal beam depends quadratically on the species concentration, which reduces with temperature, effectively reducing RCARS robustness with increasing temperature. The RCARS signal beam intensity will be elaborated upon in Section 3.6.1. Figure 3.4 shows the sensitivity of vibrational energy level population changes with respect to temperature.

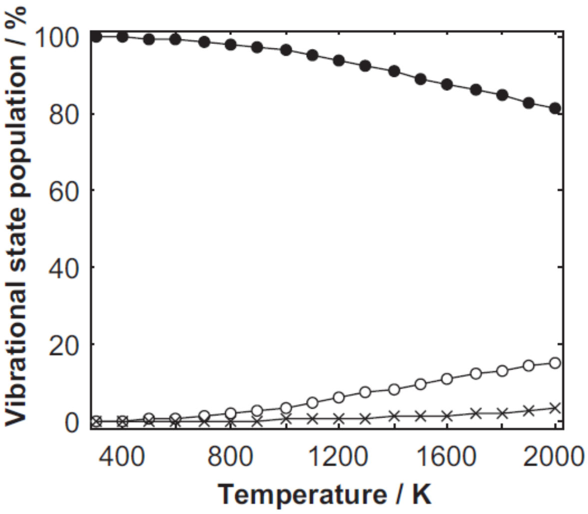

Figure 3.4: Vibrational state population of the first three vibrational energy levels with respect to temperature. The medium used is nitrogen and the relative population is given in %. Cold nitrogen only populates the first vibrational state and gradually increases with temperature. [21]

The population distribution of 3 vibrational energy levels is plotted with respect to temperature. The medium for this particular example is nitrogen. Even at temperatures as high as 800K, almost all the N_2 molecules populate the first vibrational energy level and changes in temperature barely cause a change in population distribution, making thermometry very inaccurate. Once temperatures of about 1200K are reached, changes of the population distribution with respect to temperature become more pronounced, allowing more accurate conclusions with respect to temperature. Figure 3.6, which is found and explained in detail in Section 3.5, shows that rotational energy levels are not only significantly larger in number but a lot more sensitive to temperatures changes at a wider range.

Different CARS techniques are usually classified through the energy transitions that are induced. Rotational energy transitions are denoted with ΔJ, vibrational energy level transitions with a Δv. For purely rotational CARS, the selection rules for transitions are denoted as shown in equ. 3.3.

$$\Delta v = 0, \quad \Delta J = \pm 2 \tag{3.3}$$

Here, $\Delta J = 2$ denotes transitions in the so called S-branch (anti-Stokes) and $\Delta J = -2$ denotes transitions in the O-branch (Stokes), while $\Delta v = 0$ prohibits transitions of vibrational energy levels. A signal generated under these conditions can be found in Fig. 3.5.

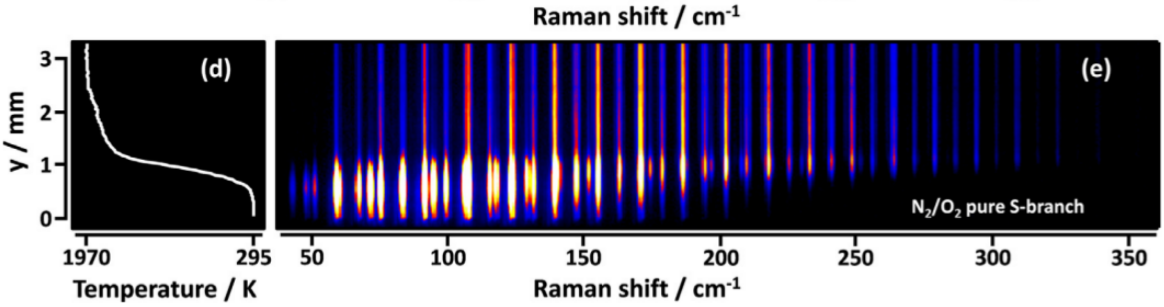

Figure 3.5: Nitrogen and Oxygen pure S-branch transitions as seen by a camera. Each distinct line corresponds to a transition from one rotational energy level to another.

Here we can see a signal generated using broadband RCARS spectroscopy on nitrogen and oxygen. Each of the spectral lines correlate to rotational energy level shift of $\Delta J = 2$. The overlap of the spectra of nitrogen and oxygen is due to the fact that the energy required to make S-branch transitions is nearly the same. Nitrogen and oxygen have a molecular weight of 14 and 16, respectively, and hence their respective molecules have a similar mass moment of inertia. This results in a similar rotational energy level spacing.

Once an accurate distribution is obtained, a library of Boltzmann probability distributions is required. Information on how to compute those can be found in Section 3.5. There is no direct way to compute a temperature from a measured distribution alone, so a common way to solve this is by computing multiple distributions of varying temperatures, for example in steps of 50K or 100K, take the sum of least squares of each of them with respect to the measured result and then plot the residual with respect to temperature. The resulting curve can be interpolated and solved for it's minimum, so the temperature at which the error would be of the least magnitude. This error is highly unlikely to ever be 0 either due to simplified models or coarse temperature grids, however this technique has been found to outperform other commonly used thermometry techniques.

3.5. THE BOLTZMANN PROBABILITY DISTRIBUTION

Once the CARS signal has been obtained, it still needs to be evaluated. In rotational CARS, the Boltzmann population distribution probability is used to derive the systems current temperature. It is a statistical method using the established relation between temperature and rotational energy level population, which enables the reading of temperature information out of spectral data. It is the essential tool which makes CARS spectroscopy into a thermometry technique.

A system in thermal equilibrium has a characteristic distribution of populated rotational energy levels. These distributions mainly depend on the species observed as well as the system's temperature. The population probability for each state can be calculated using the normalized Boltzmann factor, which can be computed using equ. 3.4:

$$P(J) = \frac{1}{Z} e^{\frac{-E(J)}{k_B T}}, Z = \sum_J e^{\frac{-E(J)}{k_B T}} \tag{3.4}$$

with k_B as the Boltzmann constant, T the systems equilibrium temperature, $E(J)$ the state energy with respect to the rotational quantum number J and Z as the sum of Boltzmann factors across all populated rotational states J. The state energy $E(J)$ is determined using eqn. 3.2. Using Nitrogen as an example, the relation between temperature and population distribution can be easily visualised. One such example can be seen in Fig. 3.6, where the probability distributions for nitrogen have been plotted for Temperatures between 300K and 2000K in steps of 100K.

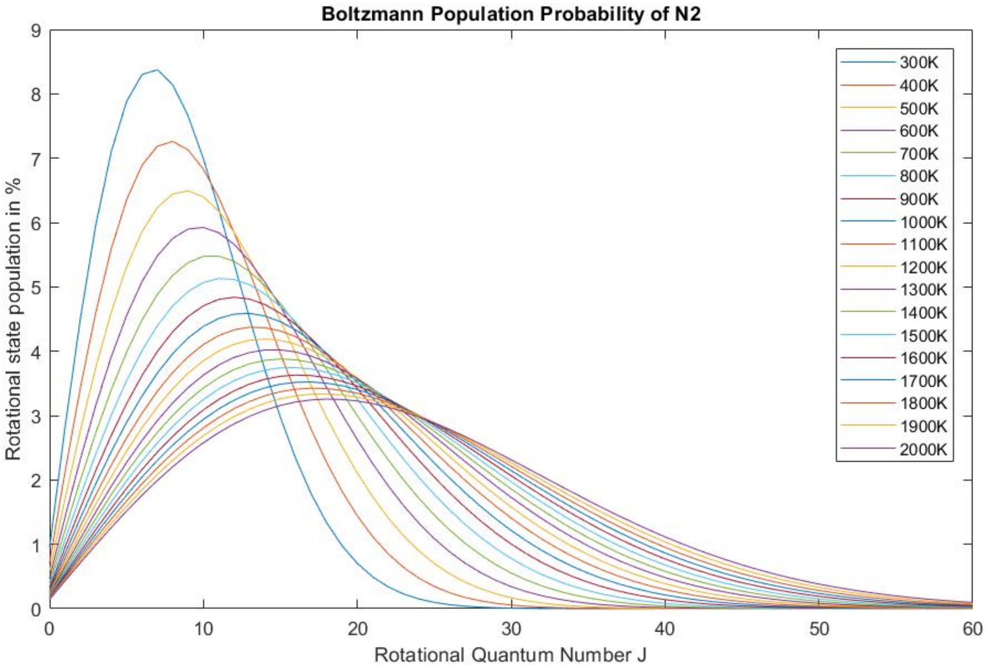

Figure 3.6: Boltzmann probability distribution for nitrogen with respect to temperature. Population probability in % on the y-axis, rotational quantum numbers on the x-axis. A widening and right shift of the spectrum as well as a reduction of the maximum population with increasing temperature are observed.

On the x-axis, the rotational quantum number J, denoting a rotational energy level, is shown. On the y-axis, the corresponding population probability of a respective state is given in %. The resulting distribution of the rotational energy level population is shown for temperatures ranging from 300K to 2000K in steps of 100K. The medium used is nitrogen. Several changes with respect to temperature can be observed. Firstly, the maximum population of the highest populated state decreases with an increase in temperature. Secondly, the quantum number of the highest populated state increases with temperature. Lastly, the spread of populated energy states increases with temperature. Overall, the amount of states populated increases and the entire distribution shifts towards higher energy levels with increasing temperature. The population difference between the populated states decreases with an increase in temperature.

It should be noted that all of these temperature dependant changes decreases with an increase in temperature. The difference between the 1900K and 2000K distribution is less pronounced than the difference between 300K and 400K, meaning the technique loses sensitivity with increasing temperature. Slight errors in the relative population measurement can therefore cause more significant thermometry errors the higher the temperature of the probe volume is. Depending on the molecule which is being investigated, pure RCARS becomes infeasible beyond a certain temperature as the population difference can no longer be accurately distinguished.

Fortunately, the temperature range experienced in the experiment that drives the thesis is compatible with purely rotational CARS, thus vibrational energy levels are not going to be elaborated any further than this.

3.6. THE APPLICATION OF CARS

After having established the theoretical groundwork and the underlying physics of generating a CARS signal, this section elaborates on some of the most important aspects to consider when setting up an experiment involving CARS spectroscopy. First, the signal intensity, how it can be computed and how certain combustion parameters affect it is elaborated. Subsequently, a more detailed explanation on recent advancements in ultra broadband 2-beam fs/ps CARS setups is provided. Lastly, the most prominent sources for signal noise as well as some methods on how to compensate for them are presented.

3.6.1. SIGNAL INTENSITY

One of the main advantages of CARS spectroscopy is the strong, laser-like signal that is generated in the process. This is achieved through the polarisation of a dielectric medium (i.e. N_2) by the electric field (incident laser beam). This section describes how the CARS signal intensity is determined according to [21]. The positively charged nucleus is shifted in the opposite direction of the negatively charged electron cloud. This effect can be computed using the power expansion in eqn. 3.5.

$$\vec{P} = \epsilon_0 \left(\chi \vec{E} + \chi^{(2)} \vec{E}^2 + \chi^{(3)} \vec{E}^3 + ... \right) \tag{3.5}$$

where $\vec{P}$ is the induced polarisation, $\vec{E}$ the electric field applied, ϵ_0 the permittivity of free space and $\chi^{(n)}$ nth order electric susceptibility tensor. Using Maxwell's equations, the formula for computing the intensity of a CARS signal in equ. 3.6 can be derived.

$$I_{CARS}(z) = \frac{16\pi^4 \omega_{CARS}}{n^4 c^4} I_{pump} I_{Stokes} I_{Prope} \mid \chi^{(3)} \mid^2 z^2 sinc^2 \left(\frac{\Delta k z}{2} \right) \tag{3.6}$$

where ω_{CARS} is the frequency of the CARS signal, I is the intensity of the respective generating laser beams, $\chi^{(3)}$ is the third-order susceptibility, z is the distance of interaction or the probe volume length and the sinc term is a phase matching condition. Essentially, Δk is the wave vector mismatch which is, ideally as close to 0 as possible in order to optimise the efficiency of the method. Equation 3.6 indicates that the intensity of the CARS signal scales linearly with the intensities of the generating laser beams and quadratically with CARS signal frequency, the probe volume length, the phase matching condition and the third-order susceptibility. The CARS signal frequency mainly depends on the lasers used and the energy transition induced, the sinc term ideally equals to 1 and the probe volume length is mainly restricted by the scale of the experimental setup. The third order susceptibility is the degree of polarisation of a dielectric in response to an electrical field and is defined as shown in equ. 3.7.

$$\chi^{(3)} = \chi_{NR} + \sum_n \sum_J \frac{a_{J,J+2}}{\omega_{J,J+2} - \omega_{pump} + \omega_{Stokes} - 0.5 i p \Gamma_{J,J+2}} \tag{3.7}$$

with p being the pressure, ω as the respective frequencies and $\Gamma_{J,J+2}$ the full width at half maximum (FWHM) Raman linewidth. The non-resonant susceptibility χ_{NR} will be further discussed in Section 3.6.3, as it is not the part of the signal that contains the desired information and is therefore considered signal noise when it comes to CARS thermometry. The resonant susceptibility is the summation off all Raman active species n and S-branch transitions from J to $J+2$. The amplitude factor $a_{J,J+2}$ is the amplitude factor and can be computed as shown in equ. 3.8.

$$a_{J,J+2} = \frac{4}{45} \frac{N}{\hbar} b_{J,J+2} F^S(J) \gamma^2 \Delta\rho_{J,J+2} \tag{3.8}$$

where N is the number density of the probed species, $\hbar$ the reduced Planck constant (or Dirac constant), $b_{J,J+2}$ is the Placzek-Teller coefficient, F^S is the Herman-Wallis (HW) factor, γ is the polarisability anisotropy and $\Delta\rho_{J,J+2}$ is the normalized population difference in the rotational states of a particular transition. The population difference factor is defined as shown in equ. 3.9.

$$\Delta\rho_{J,J+2} = \frac{g_J(2J+1)}{Z} \left[e^{\frac{E_J}{k_B T}} - e^{\frac{-E_{J+2}}{k_B T}} \right] \tag{3.9}$$

where g_J is a statistical weight factor, Z is the internal partition function which has been explained previously, T is the temperature and k_B is the Boltzmann constant. Due to the signal intensity being proportional to the square of the 3rd order susceptibility, it's dependence on any of the parameters in equ. 3.8 and equ. 3.9 is thereby also quadratic. The number density is of particular interest here because it can be used to relate the signal intensity to pressure, temperature and density of the flame through the use of the ideal gas law. With increasing flame temperature, a quadratic decrease in signal intensity is to be expected. Especially at high temperatures, this can cause issues with the dynamic range limit of a camera, which will be further elaborated in 6 where the extend of this issue is investigated. Since the temperature does not only change signal intensity but also the shape and position of the spectral lines, the thermometric sensitivity of RCARS is mainly dependent on the amplitude of the J-specific spectral lines, as explained in section 3.5.

3.6.2. ADVANCED CARS TECHNIQUES

Since the first CARS technique has been presented, the technique has been further developed and optimised. The initially developed techniques in the 1970s, which were primarily aimed at chemical analysis, had an insufficient resolution for investigating combustion processes in addition to working with a narrow band of signal wavelengths. (chun rui hu 2012) The development of broadband CARS using femtosecond lasers for the pump and Stokes beam [22] significantly increased the amount of information that could be gathered from a single snapshot. The main reason for this is the wide range of Raman shifts which can be simultaneously induced. The width of the Raman shift spectrum determines the amount of information that can be gathered on one snapshot. Molecules with a higher moment of inertia have bigger energy differences between rotational energy levels, hence the energy difference between 2 constructive photon pairs needs to be larger as well. Fig. 3.7 shows the result of a broadband CARS spectroscopy.

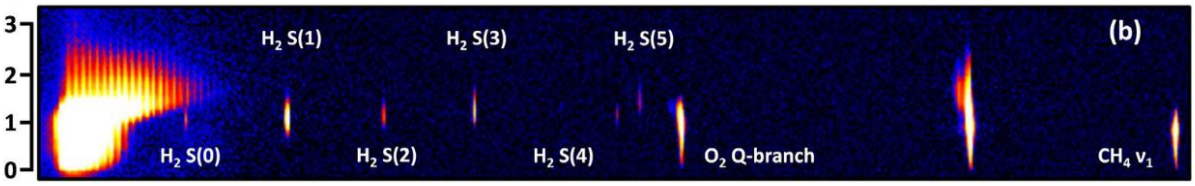

Figure 3.7: CARS excitation scheme using a broadband laser for the initial excitation on a V-flame experienceing SWQ. Raman shifts range from 0-3000 cm^{-1} on the x-axis, wall distance in mm is given on the y-axis. [23]

The spectrum displayed in Fig. 3.5 is what a zoom in on the dense series of lines seen at the left side of this spectrum would approximately look like. In addition to the Raman shifts of nitrogen and oxygen, several lines which can be attributed to hydrogen raman shifts can be found at higher wavelengths as well as a Q-branch transition of oxygen and a vibrational transition of methane. The entire rotational Raman shift spectrum of both nitrogen and oxygen does not exceed 350 cm^{-1}, whereas hydrogen transitions (denoted as $H_2S(J)$) have a significantly wider spacing. Hence the broader the spectrum of Raman shifts, the more information on the species present in the gas can be obtained using CARS. In order to maintain coherence while broadening the usable spectrum of wavelengths, the laser pulse duration has to be reduced. The so called coherence time depends on both the center wavelength of the laser as well as the bandwidth for which coherence is required. It is inversely proportional to the bandwidth. This follows the Heisenberg uncertainty principle. It dictates that the time-bandwidth product is a constant, mandating an inverse proportionality [24]. For instance, for a Gaussian shaped pulse, the relation between pulse duration and spectral width can be expressed as shown in equ. 3.10.

$$\Delta\tau \cdot \Delta\lambda \approx 0.44 \tag{3.10}$$

with $\Delta\tau$ being the pulse duration and $\Delta\lambda$ the spectral width.

In addition to using shorter laser pulses, the broad bandwidth which those lasers can produce coherently, allowed for the development of CARS techniques using only 2 lasers [25]. Instead of a separate pump and Stokes beams, a single broadband laser source is used. Figure 3.8 shows how the Raman shifts are induced using a single broadband laser as both pump and Stokes beam.

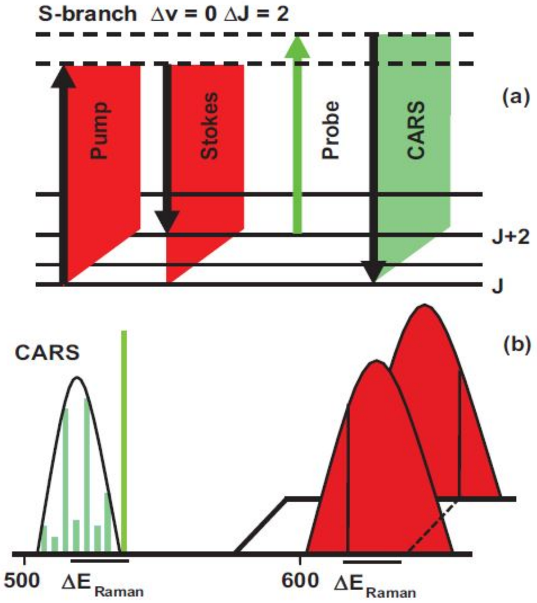

Figure 3.8: Visual representation of broadband RCARS (a) energy level excitation using a red broadband laser (b) spectral profiles of the laser beams involved. [21]

The top part of the figure illustrates how the broadband laser interacts with the varying rotational energy levels. Due to the simultaneous excitation of multiple energy levels, the probe beam, which is initially a narrow band laser source, becomes a broadband CARS signal. This is due to the fact that the single wavelength of the probe laser is shifted by multiple molecules which have experienced different Raman shifts. The lower part of the figure displays how the energy difference for the respective Raman shift is found. Within the spectrum of the red broadband laser exist numerous photons with differing energies. Whenever 2 photons who's energy difference corresponds to the energy required for a specific rotational energy level transition interact with the same molecule, this so called constructive photon pair will cause a Raman shift. Hence the largest Raman shift that can be induced using a broadband laser is equal to its bandwidth. Due to the spectrum of Raman shifts that is coherently excited, the probe laser photons are shifted by varying amounts of energy, turning the initial narrowband probe laser into an overall slightly blue shifted broadband laser beam.

3.6.3. DE-NOISING

One of the main challenges of obtaining precise results while conducting experiments on a small scale is the influence of signal noise. It may arise from the probing mechanism or the experimental setup itself, noise sources are a consequence of the combustion process itself. This section will present the most commonly encountered sources of data distortion as well as several methods to remedy or account for these issues in order to maintain adequate accuracy and precision.

Non-resonant background

As mentioned in section 3.6.1, 3rd order susceptibility can be divided into the resonant and non-resonant component. The non-resonant background signal does not contain relevant information of the combustion process and is thus deemed signal noise. One way to do remove it from the signal is by introducing a small delay between the initial pump/Stokes excitation and the CARS signal generation with the probe beam.[26] The non-resonant signal intensity decays much faster than the resonant signal intensity, so the idea is to wait until the non-resonant response has passed and then take the measurement. Studies have shown that a full suppression of the non-resonant background can be achieved when delaying the probe beam by 200ps.[27] However, the delay should not be longer than absolutely necessary. The coherence of lower rotational energy level de-phases faster than that of higher rotational energy levels. Effectively, if the probe delay is too long, the intensity of low J lines has already decayed disproportionally to the high J lines, making the spectrum look hotter than it actually is due to a seemingly high population of the upper rotational energy levels.

Laser spectral bias

In broadband CARS spectroscopy, the limited bandwidth of the laser gives rise to another source for measurement bias. When considering the fact that a constructive photon pair within the bandwidth of the same laser induces a Raman shift, it has been observed that a bias towards low energy transitions exists in the signal intensity. This can be attributed to the fact that within a finite bandwidth, there are a lot more frequency pairs corresponding to a low energy difference than a high one. In order to account for the increased stimulation of lower level rotational energy transitions, the spectrum of a non resonant gas can be used. An example of this can be found in Fig. 3.9.

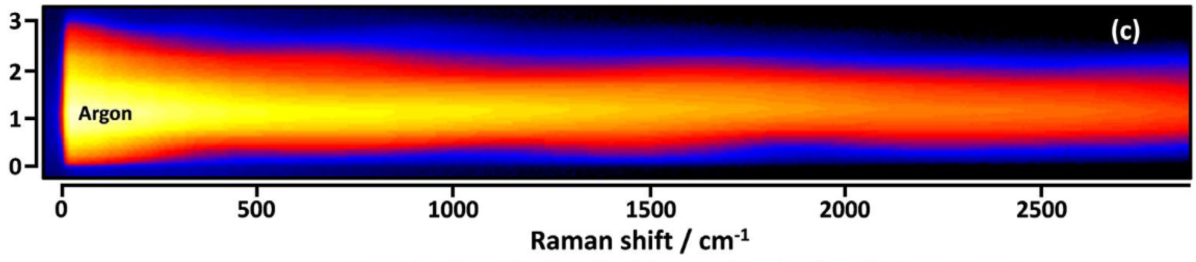

Figure 3.9: Spectrum obtained by performing CARS on argon. The lack of rotational energy levels causes a continuous spectrum of Raman shifts instead of a discrete one.

Here we can see the response of CARS spectroscopy performed on argon, however the use of any noble gas should yield a similar result. This is due to the fact that noble gases are monoatomic. As mentioned earlier, monoatomic molecules do not have discrete rotational energy levels, which means any 2 photons within the broadband laser beam can form a constructive photon pair. Since a continuous spectrum of energy differences can excite the monoatomic species, it will yield a continuous spectrum of "Raman shifts" as a response. Using this spectrum, the signal intensity reduction with respect to higher order Raman shifts can be observed. This is accounted for in the final data evaluation by dividing the resonant result with the non-resonant background.

Beam steering

One of the issues that lasers encounter when being used in combustion research is the so called beam steering. Due to the high temperatures at which the combustion process takes place, the density of the ignited mixture and the heated air around it changes significantly and with it the local refractive index. The consequence for the laser is similar to shining a light into water, the angle at which the beam progresses changes according to the refractive index, steering the beam away from the desired point of alignment. Due to CARS using at least two separate lasers, precise alignment is crucial to trigger the anti-Stokes Raman scattering. While the distance along which the beam steering can occur is small, it can still make a significant difference due to the high temperature change and the precise laser alignment requirement.

Grisch et al. placed a field lense conjugating the probe volume with the grating of the spectrometer onto the optical path to reduce shot to shot fluctuation of direction and thus minimise beam steering effects [28]. However, laser beams/sheets crossing the flame front cannot be remedied in the same way and easy solutions to this issue have not been discovered so far.

Wall reflections

Most experiments use materials like steel for the wall on to which the flame is impinging. It is relatively heat resistant and not prone to oxidation, however it causes some degree of reflection, which can affect results of the CARS signal and subsequently, the derived temperature. It has been found that the insertion of razor blades and the relay imaging of the razor edge plane onto the probe volume remedies the effects of wall reflections effectively[23]. The exact extend to which wall reflections can influence CARS thermometry accuracy and/or precision has yet to be quantified.

Acoustic Modes

Several experiments have encountered fluctuations due to acoustic modes generated by their experimental setup geometry, specifically the burner geometry [29]. Since acoustic waves are pressure waves, they can lead to small fluctuations in flame wall position or the quenching point. Due to similarities in several FWI research projects, the most commonly found value is $\pm 200 \mu m$. This corresponds to a burner cross-section of $40 \times 40 mm^2$ causing a resonance at $104 Hz$. While this can not always be remedied, it can be compensated for when analysing and processing the data. Instead of using a point on the wall as a reference point for instance, the data can be analysed for it's flame front location and aligned with respect to it. Parameters such as the quenching distance can be determined with respect to a flame specific location rather than the lab geometry, which eliminates the flame location flux issue entirely. However, there is no clear, generally applicable definition of the flame front or the quenching point of a flame, leading most researchers to come up with their own definitions. That means that accounting for the flame location flux in the data set allows comparing multiple data points in the same paper, but provides only a trend as usable information to compare to other papers since their absolute values are likely to differ if they used a different definition of the same point.

4

FLAME WALL INTERACTION

This chapter elaborates upon the phenomenon of Flame-Wall Interaction (FWI), how it comes to be, the consequences for an affected combustion process and a summary of the research done in the field.

4.1. PRINCIPLE

Most of the intentionally induced combustion processes occur in some form of a combustion chamber. These chambers are built to be very pressure and temperature resistant and contain the otherwise volatile combustion. As such, most combustion processes include FWI in some form. The advancement of technology allows for a gradual decrease in combustion chamber size while providing the same or even better performance, thus increasing the so called power density steadily. Consequently, combustion processes become more and more prone to the effects of FWI. This has several drawbacks:

- Due to cooling, walls act as heat sinks
- Due to friction, walls locally reduce flow momentum

In case of an aircraft turbine for example, combustion chambers often operate at temperatures above their materials melting point and thus employ certain cooling mechanisms to keep the structure from failing. As a consequence, heat is continuously lost to the wall. As explained in a previous chapter, the heat produced in a combustion process is not only used for energy or thrust generation, but also to self sustain the combustion process. A heat loss at the wall can cause an early quenching of the flame, and with it, local incomplete combustion due to a lack of activation energy, thus decreasing engine fuel efficiency and increasing harmful emissions.

Furthermore, the formation of a boundary layer at the wall has several aerodynamic consequences. A loss of momentum or back flow regions within the boundary layer can cause a so called flashback. A flashback is the propagation of the flame front against the main flow direction, meaning the flame moves towards the fuel/oxygen source. This can seriously damage parts of the machinery used.

4.2. PAST RESEARCH

Several studies have been performed on FWI and while there is still a lot to be done, the similarities among several of these experiments already allow for some comparisons and first conclusions.

4.2.1. COMMON EXPERIMENTAL SETUPS

First of all, the distinction is made between two types of FWI: head-on quenching (HOQ) and side-wall quenching (SWQ). As the names suggest, a HOQ experimental setup involves a flame with its flow direction normal to the wall, hence impinging orthogonally, whereas SWQ requires the core flow direction to be nearly parallel, hence 'grazing' the wall. A sketch a HOQ setup can be found on the left of Fig. 4.1, an example of a

SWQ setup can be found on the right.

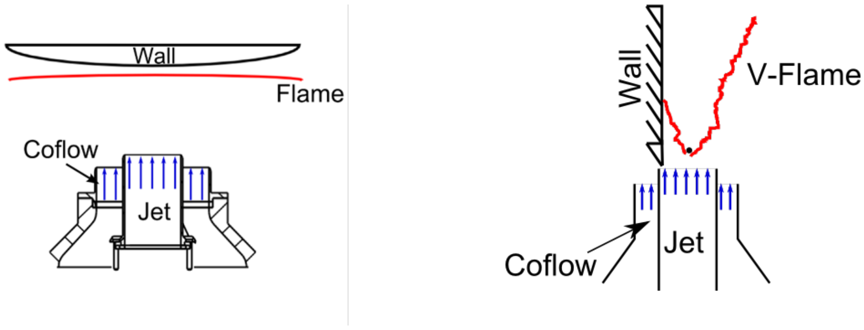

Figure 4.1: Schematic of a HOQ setup (left) and a SWQ setup (right)[30]. The fuel/air mixture (denoted "jet") is surrounded by an air coflow to prevent mixing with the ambient air. Flame front indicated in red.

Aside from the obvious geometric difference, there is also an operational difference between these setups. With a SWQ configuration, a quasi steady flame can be achieved. Once the flame is ignited, the person conducting the experiment can find the right combination of mass flow, equivalence ratio and various distance such as nozzle height in order to create a continuous FWI and take as many measurements as required at any location. HOQ however does not allow for a continuous flame, as the flame is completely extinguished due to the quenching process. The flame has to be re-ignited each time in order to take multiple measurements. This usually leads to a large number of measurements being taken and then collected in, for example, so called scatter plots. An example of such a scatter plot can be found in Fig. 4.2.

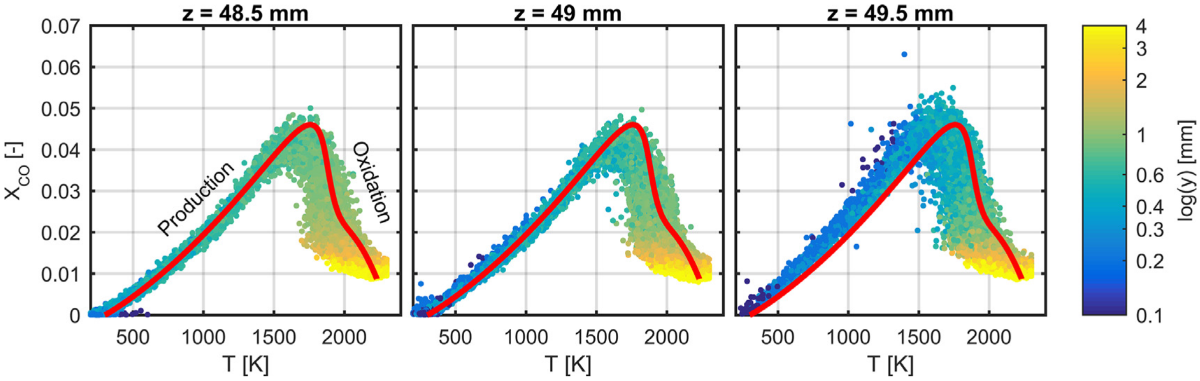

Figure 4.2: Thermochemical states of a flame in a SWQ configuration at $\phi = 1$ at varying burner heights. All wall distances are summarized in a plot. Red line represents an undisturbed laminar flame obtained from a 1D flame calculation.[12]

In this example, every point in the plot represents one simultaneous measurement of carbon monoxide concentration and temperature. Not only did this experiment take multiple measurements at the same location, but the measurement location was also varied along the path of the working fluid, a methane-air mixture in this case. If enough repetitions have been completed, certain trends can start to manifest themselves in the data despite the fact that each measuring point technically belongs to a different flame.

The thesis to be written will discuss the results of an experiment using the SWQ configuration. As with many such studies, a premixed methane/air flame is impinging on a ceramic rod with a small diameter ($\sim 1mm$), splitting it into a V-flame. This way, the flame can be discretised as a 2-D flame, removing 1 line of sight (LOS) issue. Looking at a regular flame, as seen on top of a bunsen burner for example, would make measurements complicated since the temperature is not constant along the LOS from any angle. Hence, measured data could never be clearly related to a specific location within the flame.
With the flame having a V-shape, a vertical wall can be placed next to it to induce SWQ effects. This describes

a generic SWQ experimental setup and multiple variations of this have been used to make a variety of discoveries. Due to the high complexity involved and resulting costs, most setups are designed to provide the basis for a series of experiments over many years.

4.2.2. TU DARMSTADT

One of the most prominent FWI research series was performed at the TU Darmstadt, where several experiments have been conducted on both SWQ and HOQ experimental rigs. The conclusions made in these studies will provide the main context and background information during the analysis of the data to be examined. The sample layouts for SWQ and HOQ experimental setups were taken from 2 of the papers of which the results are presented in the following paragraphs. This section discusses 5 papers specifically investigating the effects of FWI, most of which make some conclusions regarding turbulence. First a quick overview is given regarding which paper conducted what kind of experiment, followed by a summary in which the results from all 5 papers are correlated. While some results were only obtained in one of the 5 papers, others reconfirmed previously found phenomena or found complementary information that confirms previous results by effectively completing the picture.

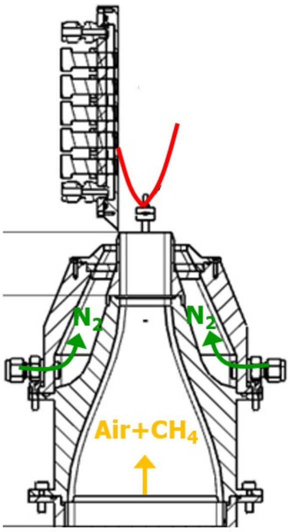

Figure 4.3: Schematic of the SWQ burner setup used by the TU Darmstadt combustion research group. A methane-air mixture passes through a morel shaped nozzle and is surrounded by a nitrogen coflow upon exiting. The ceramics rod functions as a flame anchor and causes the flame to assume a V-shape. The left flame branch is quenched by a wall.

The burner schematic shown in Fig. 4.3 describes the burner used for the SWQ configuration in detail. A methane air mixture is lead through a morel shaped nozzle. Upon exiting, it is surrounded by a nitrogen coflow in order to inhibit mixing with the ambient air. This preserves the mixing ratio of the working fluid. The flame is anchored using a ceramics rod, which causes the flame to assume a V-shape. The left flame branch then impinges on a water cooled wall, where it is subjected to various measurement techniques.

THE PAPERS

While all of the papers generally used one of the previously displayed experimental setups, they differed in how the flame was investigated. Below is a rough summary of the experiments conducted in chronological order. Table 4.1 sums up the most essential similarities and differences in terms of the experimental setup and the parameters investigated.

The first paper [31] investigated spectroscopic temperature an CO radical concentration measurements in order to investigate transient FWI. The HOQ setup used nitrogen CARS spectroscopy for instantaneous temperature measurements and simultaneous two-photon LIF. The experiment was conducted at 3 different equivalence ratios, one lean, one stoichiometric and one rich and each of those have been repeated at both laminar and turbulent conditions. Due to the nature of HOQ, 200 repetitions were made of each experiment and gathered in T/CO scatter plots for evaluation. In addition, wall heat transfer was computed out of wall

Paper	[31]	[32]	[33]	[34]	[35]
SWQ		X	X	X	
HOQ	X				X
PIV		X		X	X
OH-LIF		X		X	X
CO-LIF	X		X		X
PT	X		X		X
CARS	X	X	X	X	X
Lean	X	X		X	
Stoichiometric	X	X	X	X	X
Rich	X			X	
Laminar	X	X	X	X	
Turbulent	X	X	X	X	X
CH_4	X	X	X	X	X
C_2H_4					X
CH_3OCH_3			X		

Table 4.1: Tabulated summary of essential experiment characteristics.

temperature data gathered through phosphor thermometry (PT).
The second paper [32] investigated the effects of FWI on flame surface density as well as the mean reaction rate. Here, a SWQ setup was chosen. Using PLIF, the concentration of OH radicals was measured along the path of propagation of the quasi 2-dimensional V-flame. Additionally, PIV measurements provided information on the flame flow field. A direct comparison as made to previously conducted DNS studies, which the experiment aimed to validate. A lean and a stoichiometric equivalence ratio were investigated in both laminar and turbulent conditions.
The third paper [33] used a HOQ setup to investigate flame-flow interactions of premixed turbulent flames. The flow field was tracked with PIV, while OH-LIF was used to track combustion phases and identify quenching locations. Only stoichiometric conditions were investigated, however 2 different fuels were used: methane (CH_4) and ethylene (C_2H_4).
The fourth paper [34] investigated the effects of quenching due to FWI on the local flow field. PIV and OH-LIF were the techniques chosen to investigate the flame once more, setting up two measurement planes on a SWQ setup. Additionally, pointwise CARS spectroscopy was applied in order to record gas temperatures. Here, the focus lies on Reynolds stresses and the production term of turbulent kinetic energy. What separates this experiment from the others is the comparison of the reacting flow to a non-reactive case, meaning a Flow-Wall Interaction of the same gas mixture but without the ignition. Again, 3 equivalence ratios were used (lean, stoichiometric and rich), however only at turbulent conditions.
The last paper discussed in this section [35] used the SWQ setup to investigate both wall heat fluxes and CO radical formation/oxidation. CARS spectroscopy was used for gas temperature measurements, two-photon LIF for CO concentration measurements as well as phosphor thermometry for wall temperature tracking. Additionally, OH-PLIF was applied for flame front tracking. The experiment was conducted at both laminar and turbulent conditions and investigated 2 different fuels, methane and dimethyl ether (CH_3OCH_3).

All of these papers used premixed flames, meaning air and fuel were mixed pre-ignition, and applied active cooling to the walls used to quench the flames in order to keep them at a constant temperature. Wall temperature tracking was applied in order to either guarantee constant wall temperatures or to be able to derive wall heat fluxes, which depend on the temperature difference between the wall and the flame. Due to the similar fashion in which parameters such as quenching point and flame front were defined and tracked, the results are easily comparable and relatable to each other.

Findings Summary

One of the most relevant aspects of FWI that was investigated was the influence of turbulence. As to be expected, it has numerous effects on vital combustion parameters such as temperature and (radical) species distribution. To start with explaining these differences, it is best to start with looking at the shape of the flame itself, which can be achieved through both PIV and (P)LIF measurements. The latter mostly determines the state of the flame (flame front, oxidation zone a.s.o.) whereas PIV provides the flow field. It has been found that turbulence causes an increase in flame wrinkling. Flame wrinkling can be most easily explained by visualising the difference between a blowtorch and a camp fire, the blowtorch not showing any obvious wrinkles in the flame and the camp fire being heavily wrinkled. These wrinkles effectively increase the surface area of the flame. Additionally, Rißmann et al.[35] found that there seems to be a correlation between the Lewis number and the intensity of flame wrinkling, though this influence has not been quantified yet. Due to the lack of uniformity of a turbulent flame, local heat fluxes can occur. A sudden variation in temperature causes a change in either density or pressure, if not both. This has been found to directly influence the flow field, causing slight disturbances to the velocity as well as the flow direction with respect to the laminar case. Though it has not been explicitly stated, this could be perceived as flame wrinkling. Another effect on the flame geometry stems from the type of fuel used, which has been simply attributed to the difference in laminar flame speed.

In terms of temperature and species profiles, turbulence tends to flatten them out. This usually implies that the maximum in the temperature and emission profiles is lower than for a laminar flame and not focused on one small location but rather spread out across a longer section of a wall. This is the first of multiple experimental results that illustrate the relation between local temperature and the presence of certain species. Experiments using a HOQ setup have found that turbulence causes a blurring between the main reaction zone and the oxidations zone of the flame, introducing 'intermediate states' that would not be present in the laminar case. The mixing of these combustion phases (locally speaking) could explain why the temperature profile shows more of a plateau shape around its maximum. If a clear relationship between temperature and species concentration can be established, the influence of turbulence on species concentration could be derived solely from temperature measurements of FWIs, avoiding the necessity to design experiments that employ multiple measurement techniques simultaneously. This is clearly desirable, as synchronising multiple different techniques in one experiment does not only cost additional time and money, but may also give rise to measurement errors due to adverse interferences.

Another way the similar behaviour of species concentration and temperature as a response to turbulence can be observed, is by investigating the boundary layer at the wall. The shape of carbon monoxide and temperature plots in the boundary layer has not only been found to correlate quite well, but to experience similar changes once turbulence is introduced as well. It is not as well observable in the boundary layer as it is in the free flame though, because turbulence has been found to decay close to the wall, gradually assuming a more laminar shape. Beyond the quenching point, a completely laminar boundary layer seems to develop despite the initial turbulence of the flow. The observation can be made not only in terms of flow direction and velocity, but also with respect to the species and temperature profiles, which gradually become more similar to the results of laminar flow investigations. This fits with the findings of Rißmann et al.[35], which confirmed DNS calculations that predicted less flame wrinkling during FWI due to increased Lewis numbers.

This is especially interesting when considering heat transfer to the wall, as a turbulent boundary layer would allow for more heat transfer than a laminar boundary layer. This can be attributed to vortices mixing the hot gas far from the wall with the already cooled down gas close to the wall. However, results indicate that the heat transfer to the wall is actually reduced for the turbulent case. It is not exactly clear why turbulence decays along the wall, however Jainski et al.[34] found that this does not happen for an non-reacting flow. Impinging the cold gas onto the wall results in a turbulent boundary layer, the continuous laminarisation only occurs once the mixture is undergoing combustion.

Focusing more on the aspect of species concentration and temperature, observations can be made that tend to confirm intuitive expectations. For instance, close to the wall the temperature drops steadily, more so than in the free stream, leaving a higher concentration of CO radicals which escape through the boundary layer without reacting. This is not only undesirable from an emission point of view but also affects the overall fuel efficiency of a potential combustion chamber. The oxidation of carbon monoxide contributes to the release of additional heat. This effect is only amplified in fuel rich conditions, which already suffers from excess radicals in the exhaust due to the lack of oxygen.

Lastly, a few conclusions were made with regard to the current state of direct numerical simulation (DNS). One could argue that the main goal of experimentation is to further the understanding of the physics behind the combustion process in order to create accurate models that can be used to optimally design combustion chambers. Hence an idea of where these models are still lacking can help to set priorities with respect to which parameters and/or phenomena need to be investigated. Overall, there haven't been too many definite conclusions made in these specific papers, however Kosaka et al.[33] found that the radical oxidation region of the combustion can be predicted sufficiently using laminar 1D calculations, however the simulation is off when it comes to the initial radical formation at and close to the wall. For the turbulent case, no definite conclusions were made other than that the flow field around the quenching point is can be accurately reproduced using DNS, leaving this question considerably unanswered. While it would exceed the thesis scope to investigate this as well, there is definitely a need for additional model validations.

5

SANDIA EXPERIMENT

This chapter presents one of the most recent applications of CARS thermometry in the assessment of FWI. An experiment has been conducted at Sandia National Laboratories for which a two-beam broadband 1D-CARS spectroscopy setup has been developed and built. It has been used to conduct a thermometry investigation on both laminar and turbulent FWI in a line across the flame front. The ultrafast femtosecond pump/Stokes laser allows for a broad excitation of energy states and the capture of an entire rotational energy spectrum in a single snapshot. This chapter explains how the experiment was conducted and presents some of the results as well as their implications on FWI.

5.1. EXPERIMENTAL SETUP

This section elaborates upon the burner and the optical setup as well as the operational capabilities/limits.

5.1.1. BURNER

The burner setup follows the generic SWQ design presented in chapter 4. A mixture of methane and air enters a settling chamber, from which it enters a duct featuring two fine meshes as well as a honeycomb structure, which homogenise the mixture. It leaves the duct through a morel shaped quadratic jet nozzle with a cross-sectional area of 40 x 40 mm^2 at the exit. The sharp edges of the nozzle minimise the recirculation zones and the contoured nozzle provides the mixture with a top-hat exit velocity profile. The burner geometry causes Helmholtz resonances at a frequency of 104Hz, which results in vertical fluctuations of the flame tip of $\pm 200 \mu m$.

The air co-flow surrounding the central flow exiting the duct at 75% of the bulk velocity prevents a mixing of the ambient air and the fuel/air mixture between nozzle exit and flame anchor. The flame anchor is a ceramic rod with a diameter of 1mm and is located 16 mm downstream the nozzle exit. The wall which interacts with one of the resulting flame branches is water cooled in order to maintain a constant temperature throughout the experiment. A slight curvature with a radius of 300 mm provides optimal optical access for the CARS lasers.

All experiments are conducted at a Reynolds number of 5000, which is computed using the hydraulic nozzle exit diameter as the characteristic length. Additionally, the equivalence ratios investigated consist of a lean, a stoichiometric and a rich fuel mixture of $\Phi = 0.83, 1$ and 1.2, respectively. Additionally, a turbulence grid can be added to the duct after the mixture is homogenised.

5.1.2. OPTICAL

The experiment uses a newly developed two-beam 1D-CARS configuration. It allows for the probing of rotational and vibrational (O-, Q- and S-branch) energy transitions of N_2, H_2, CO_2, O_2 and CH_4.

Figure 5.1 shows a schematic of the 4-f optical arrangement used in this experiment. The pump/Stokes beams are broadband laser sheets emitted from the same laser source with a bandwidth of $400 cm^{-1}$. This broad bandwidth is achieved by using an ultrafast laser with a pulse length of 45fs. The line of intersection of these sheets is the measurement location. The hereby induced energy level transitions are probed using a narrowband probe laser with a pulse length of 75ps. The signal is then relay imaged through a short pass filter in order to separate the co-propagating probe beam from the CARS signal beam. Finally, the signal beam is

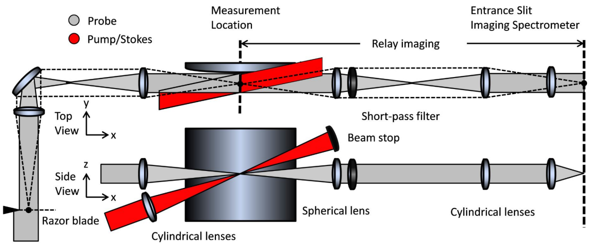

Figure 5.1: Schematic of the laser arrangement as used in the experiment. The pump/Stokes beam intersects with the probe at the measurement location and is relay imaged to the entrance slit of a spectrometer using a 4f-correlator

relay imaged onto the entrance slit of an imaging spectrometer, where the varying frequency components of the signal are spatially separated and captured by a CCD camera.

5.2. DATA EVALUATION

The snapshots captured by the CCD camera have to be processed and evaluated in order to obtain temperature data. This is done by using two matlab scripts. This section describes how the CARS signal is processed, relevant inputs and assumptions used in the code.

5.2.1. IMAGE PROCESSING

The first step is the conversion of the CCD camera image into numeric values of local signal intensity. The example images shown here are the result of measurements taken at 44mm above the burner nozzle and a probe pulse delay of 240ps.

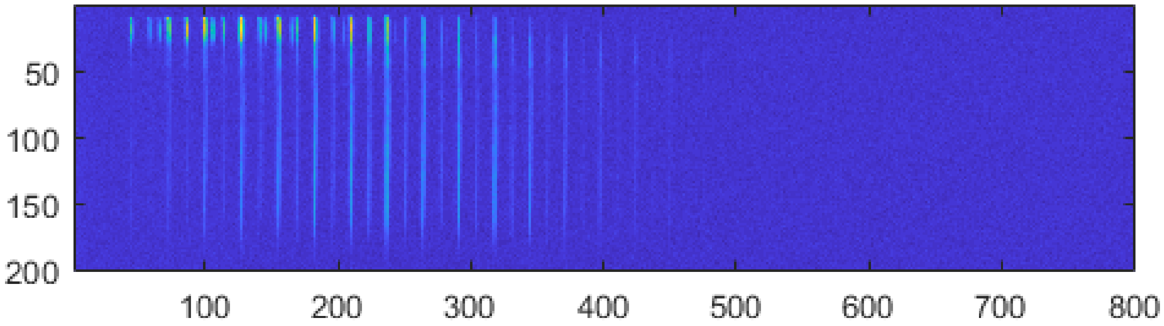

Figure 5.2: CCD camera image of a nitrogen RCARS spectrum. Brightness/intensity is used to assess relative population. The y-axis represents wall normal distance in mm and the x-axis the Raman shifts in cm^{-1}

Figure 5.2 is an example of a CARS spectrum as captured by the CCD camera. The y-axis represents the line along which the measurement was taken (0-2mm from the wall) and the x-axis represents range of signal components in terms of wave number. Due to the wavenumbers and distances from the wall only being applied to the image later, the units on both axis are given in pixels. The code isolates a line of these pixels corresponding to a certain wall distance and converts the brightness of each pixel into an intensity value. An example of four such intensity spectra can be seen in Fig. 5.3.

Here four different spectra are taken out of the image at varying distances with respect to the wall. The x-axis represents the wavenumber and the y-axis the corresponding intensity. The code will normalise the intensity spectrum down the line, making the maximum value exactly 1 because only the relative population is relevant for the spectral fitting routine. However, even though the absolute value of the maximum intensity doesn't provide a lot of information by itself, a comparison between the four images already reveals several things. Firstly, the maximum intensity seen in Fig. 5.3d is multiple times larger compared to the other images, meaning this is the coldest region captured by the image and thus the location immediately next to the wall where the combustion hasn't taken place yet. The narrow population distribution is indicative of this as well, since molecules in cold gases only populate lower order rotational energy levels. At the immediate edges of the image, both at maximum and minimum wall distance, the image contains mostly signal noise,

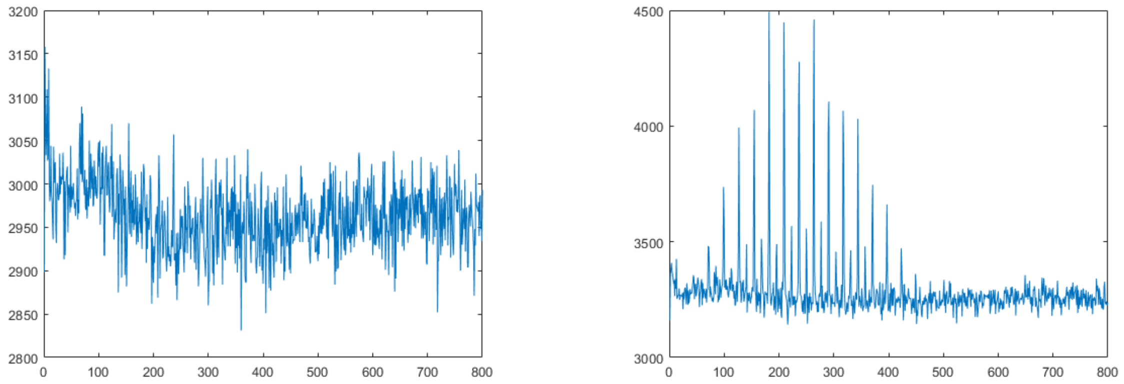

(a) CARS spectrum measured at 2mm wall distance.

(b) CARS spectrum measured at 1.9mm wall distance.

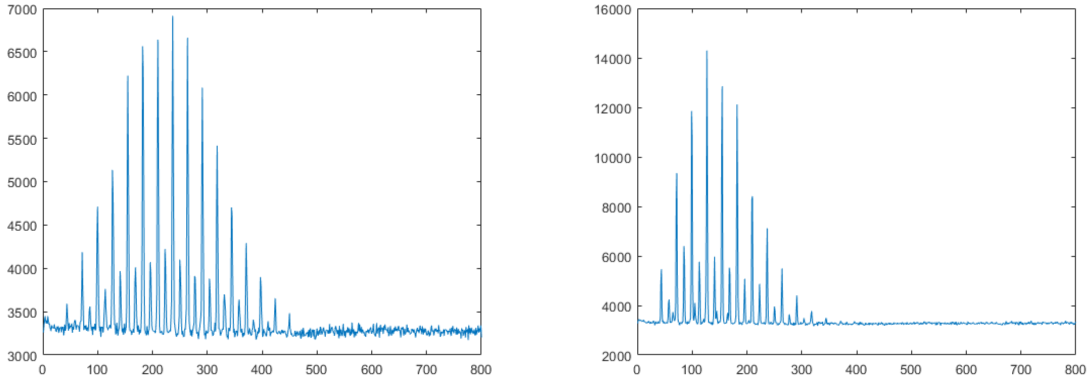

(c) CARS spectrum measured at 1mm wall distance.

(d) CARS spectrum measured at 0.1mm wall distance.

Figure 5.3

as shown in Fig. 5.3a. The influence of this noise can still be seen in fig 5.3b however despite being present, it hardly shows up in Fig. 5.3d. This is also tied to the difference in intensity, since the signal noise intensity remains relatively similar, the cold CARS intensity spectra are much less affected than the hot CARS spectra. This will be addressed again in 5.2.3 when a temperature profile is generated out of this series of CARS spectra.

In order to improve spectral fitting accuracy, each peak is integrated and saved as a singular intensity value per wave number. By comparing this spectrum to a spectral library, the flame temperature at this specific wall distance can be derived. The following is a description of what a spectral library is and how it is generated.

5.2.2. SPECTRAL LIBRARIES

Spectral libraries contain a series of theoretical CARS spectra which are computed based on the CARS theory presented in chapter 3. The code used for the data evaluation of the experiment described in section 5.1 computes the CARS spectra for nitrogen at temperatures ranging from 200K to 2400K in steps of 100K. In addition to the respective temperatures, required inputs are the probe pulse duration in ps, the probe pulse delay in ps and two libraries. The first library contains measured linewidths of nitrogen. The linewidth library only contains data for temperatures ranging from 300K to 1400K, linewidth below or above this threshold are computed. The scaled linewidths are computed using eqn. 5.1.

$$LW_{N2_{scaled}} = LW_{N2_{1400}} * \frac{1400}{T}^{0.704}; \tag{5.1}$$

Here, $LW_{N2_{1400}}$ is the linewidth corresponding to a temperature of 1400K, T is the temperature for which a linewidth is to be computed and 0.704 is a scaling exponent. For a library generated at 200K, the entry corresponding to a temperature of 300K is used for scaling instead.

The second library contains a list of transition energies corresponding to the first 60 rotational energy level transitions. These are the wave numbers with which the integrated Raman shift peaks of the spectral libraries and the measured CARS signal are correlated.

The energy response induced by CARS lasers is computed using eqn. 5.2.

$$E_{CARS}(t,\tau) = E_{probe}(t-\tau)\cdot \sum_{J=0}^{J_{max}} \Lambda_J e^{(i\Delta E_J - \Gamma)\frac{t}{\tau}} \tag{5.2}$$

This equation computes the electrical field induced by the CARS signal. By computing the Fourier transform of this field, the frequencies of this signal and their relative intensities are obtained.

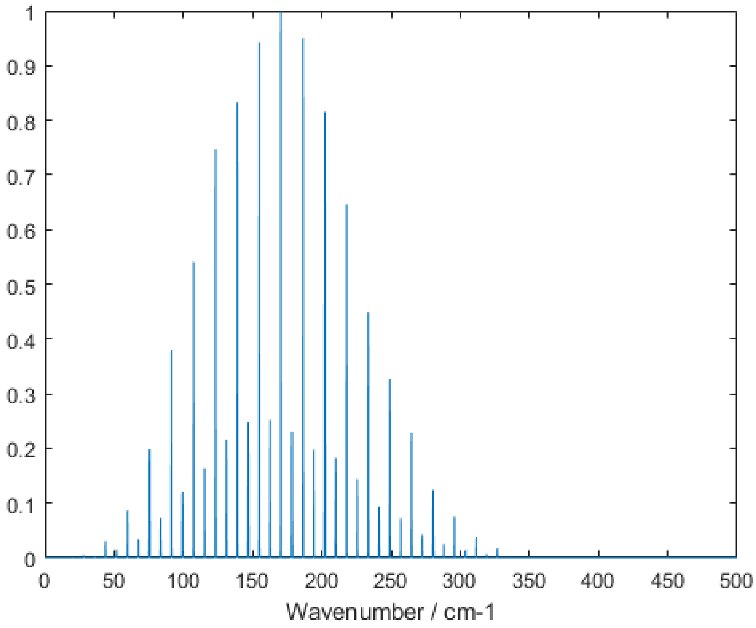

Figure 5.4: CARS electrical field strength as computed by Matlab code. Probe pulse delay of 260ps, probe pulse width of 100ps Temperature of 1000K. Peaks are integrated before the spectrum is added to the spectral library.

On the x-axis, the wavenumber of the respective Raman shifts is displayed in $\frac{1}{cm}$ and on the y-axis the relative CARS signal intensity is displayed. This spectrum is generated assuming a probe pulse width of 100ps and a probe pulse delay of 260ps. The temperature resulting in this spectrum is T = 1400K. Lastly, each peak is integrated and summed up into one value per rotational quantum number. Hence the data which is compared by the SSQ routine does not compare the shape of the spectral lines but only the absolute values. One such array of values per quantum number is added into the spectral library for each temperature.

5.2.3. SPECTRAL FITTING

With the spectral libraries computed and the CCD image processed to fit the format, the temperature data can be computed. This is done by applying the sum of squares method. For each temperature in the library, the difference between the measured and the computed peaks is squared and summed up. This correlates each temperature in the library with an error value. Plotting this error value against the temperatures yields a quadratic function as illustrated by Fig. 5.5.

The x-axis lists the temperatures of the spectral library while the y-axis shows the residual error of the sum of squares method. By interpolating this graph and recomputing it with a fine temperature grid (using steps of 0.5K), the minimum of this function can be found. The temperature corresponding to the minimum residual error is the final result and output temperature of the spectral fitting routine.

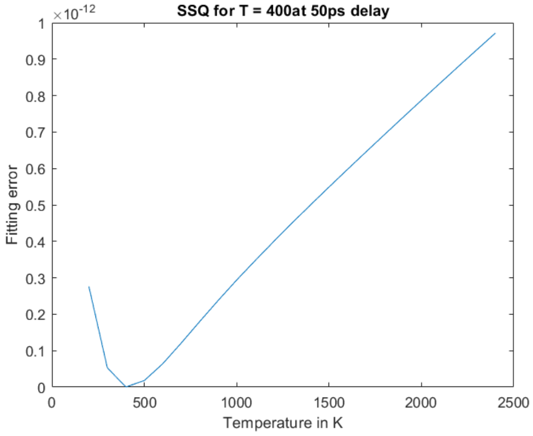

Figure 5.5: Illustration of the SSQ method as applied by the spectral fitting routine. The library temperatures are shown on the x-axis and the corresponding residual errors are on the y-axis.

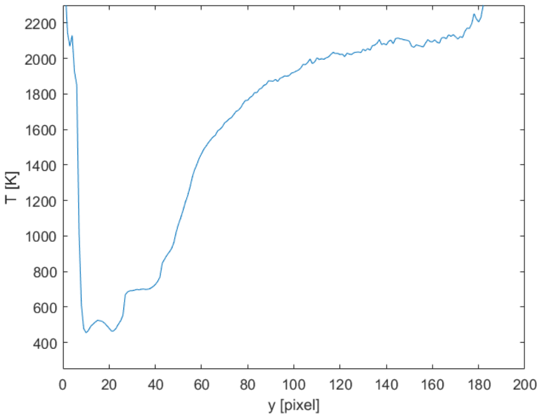

Figure 5.6: Temperature profile of FWI CARS measurement taken at 44mm above burner and 240ps probe pulse delay. The wall distance is shown on the x-axis (200 pixels ≡ 2mm) while the corresponding temperature is shown on the y-axis.

In Fig. 5.6, the resulting temperature distribution is shown for the example used in 5.2.1. The wall distance is shown on the x-axis and the corresponding temperature is shown on the y-axis. The first noticeable thing of this distribution is the unusually high temperature right next to the wall. This can be attributed to the signal noise shown in Fig. 5.3a being relatively uniformly distributed. The SSQ routine associates this with high temperatures due to the population distribution of CARS spectra becomes broader and flatter the hotter the probe volume is. This is simply removed in post processing as it marks the boundary at which spectral information can be obtained due to the wall being present.

5.3. TURBULENT FLAME WALL INTERACTION

An experiment has been conducted on the effect of turbulence on FWI. As the results of the studies presented in chapter 4 have shown, laminar and turbulent FWIs show significant differences when it comes to heat release/loss as well as combustion product formation. The investigation of turbulent FWI in the experiment presented here has revealed significant differences to the laminar investigation which will be elaborated upon in this section.

The experiment consisted of 3 measurement series, using a lean, a stoichiometric and a rich gas mixture. During each measurement, the measuring height above the burner was varied from X mm to X mm (in steps of X mm).

Figure 5.7 shows the results of a measurement series consisting of 500 snapshots of a turbulent FWI. The measurements are taken at a height of 42mm above the burner and the fuel mixture used was stoichiometric. In the top left, a picture of the flame is shown. The dashed white line indicates the measurement height,

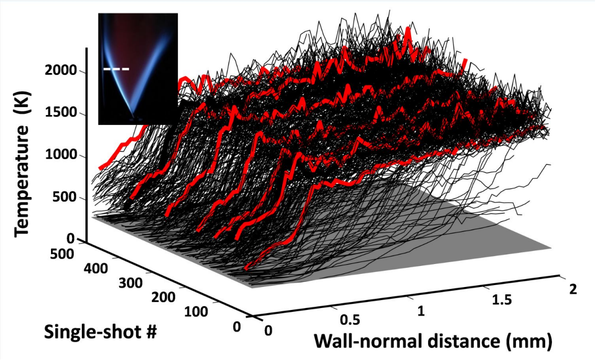

Figure 5.7

which is located several mm below the flames point of contact with the wall (and thus, the quenching point). It should be noted that, despite not making direct contact with the wall, the entire flame branch is affected by its presence. The right branch is a freely propagating flame and differs in both propagation angle and flame thickness. Additionally, while the flame branch interacting with the wall assumes a slight curvature, the freely propagating flame remains relatively straight. This indicates that FWI affects a much larger part of the combustion process and not just the physical point of contact between flame and wall.

For each snapshot (z-axis), the temperature (y-axis) is plotted with respect to the wall-normal distance (x-axis). The red measurement lines are selected randomly and are only intended to improve readability. While further data processing has revealed more than this plot can show, several things can already be observed here. Firstly, while most measurements seem to follow a similar trend of starting around 500K, quickly rising to temperatures beyond 1500K and settling at some temperature between 1500K and 2000K, this is not the case for every measurement. Some snapshots show temperatures barely exceeding 300K (wall/ambient temperature), suggesting that neither combustion nor preheating has occurred yet. Additionally, some exceedingly hot measurements can be seen as well. This is indicative of a turbulent combustion process, as even a steady SWQ setup cannot maintain a fixed flame front location.

A behaviour which, so far, remains unexplained, is the temperature spike of the flame front after which the temperature quickly drops, sometimes by several hundred Kelvin. This behaviour has not been observed in any of the laminar FWI studies and does not fit the general S-curve behaviour of heat release presented in chapter 2. This behaviour is further examined in Fig. 5.8.

Figure 5.8a shows the scatter plot of temperature gradients with respect to wall normal distance of the data presented in Fig. 5.7. The gradients are taken of each snapshot where the combustion process reaches 1000K. While this mostly occurs between 0.1mm and 0.5mm distance from the wall, the turbulent nature of the combustion process causes this point to occasionally occur much further away from the wall or even not at all.

The red dots indicate the maximum temperature gradients observed in an equivalent experiment on laminar FWI. Due to a significant amount of turbulent measurements exceeding this maximum, these snapshots are subject to further investigation. Figures 5.8b, 5.8c and 5.8d show only the measurements which have a temperature gradient of 120K/bin at the 1000K location (corresponding to the highlighted area in Fig. 5.8a). They use the same height above the burner and mixing rations of 0.8, 1 and 1.2, respectively. The red line indicates a calculated average of all the data points included.

The stoichiometric and rich mixtures cause such high temperature gradients significantly more often than the lean mixtures and the temperature spike at the flame front is barely noticeable in the average temperature profile. However the plots for stoichiometric and fuel rich mixtures feature a clearly visible temperature peak. While the release of heat is not necessarily surprising, it is not clear where all the thermal energy escapes to in order to create such a significant temperature drop. A possible explanation could be enhanced mixing of the hot reacted mixture with the ambient air due to the turbulence. If mixing between the reacted mixture and the cold zones next to the wall is enhanced, more thermal energy is lost to the wall.

Another observation regarding turbulence can be made when comparing the pattern of the temperature profiles with varying height above the burner.

Figure 5.9 shows a series of snapshots the turbulent, stoichiometric FWI at 52mm, 58mm and 64 mm above burner, respectively. At lower heights, the spread of the temperature lines is relatively wide, showing both complete combustion and preheating conditions at the same location. However as the measuring height above the burner is increased, the spread decreases significantly and the temperature lines become more similar to each other. This could be indicative of the wall induced relaminarisation of the flow or a flame front position fluctuation as suggested by the research presented in chapter 4. Additionally, when comparing the lean and more fuel rich cases, it was found that the deviation of the measured temperature profiles (as seen in Fig. 5.9) increases with an increasing mixing ratio. The stoichiometric and fuel rich cases, which behaved relatively similar to one another, show a bigger deviation between each measurement at a given height above the burner (HAB). The less "volatile" nature of the lean flame suggests that the impact of turbulence on FWI, or even flames in general, depends on the mixing ratio as well.

In order to investigate these hypothesis, an additional set of plots has been generated with focus on flame position and flame progress with respect to the HAB.

Figure 5.10 contains 3 plots used to gain a different perspective on the data presented so far. Firstly, in fig 5.10a, the progress variable for all 3 mixing ratios with respect to HAB is shown. The reaction progress is defined with respect to the temperature gradient, where a temperature gradient of 0 indicates a complete or quenched combustion process which no longer releases heat. The fuel lean mixture reaches this point significantly earlier than the stoichiometric and fuel rich mixtures, which is to be expected due to the fact that less fuel is available overall.

Secondly, in fig 5.10b, the 1000K isotherm for each of the mixing ratios is shown with respect to the HAB. While the behaviour is relatively similar, In addition to that, the respective temperature gradient at this 1000k isotherm has been plotted with respect to the HAB as well, as can be seen in fig 5.10c. In all cases it can be observed that the 1000K isotherm moves closer to the wall as it propagates downstream of the burner, converging towards a minimum distance of about 0.15-0.2mm. The temperature gradient continuously decreases, indicating a constant reduction of heat release, which is to be expected as the combustion process goes on. The lean flame shows overall less heat being released, which aligns with the relationship between heat release and mixing ratio previously established in chapter 2 Note that for both of these plots, the measurement line for the lean ($\phi = 0.8$) cases has been shifted by 13mm in order to fit on the same graph and illustrate the similar behaviour. However despite showing a similar HAB dependence, a clear difference between the lean case and the stoichiometric/rich cases can be observed while the latter two appear to hardly vary from one another.

The flame angle and flame speed depend on the mixing ratio and influence the upward vertical shift of the area of contact between flame and wall as the mixing ratio decreases below stoichiometric conditions. However, the laminar flame speed of methane is maximised at stoichiometric conditions and decreases for both increasingly rich and lean mixtures [36]. The fact that there is hardly any difference between stoichiometric and rich fuel mixtures (relatively speaking) implies that either:

1. Turbulence changes the relationship between flame speed and mixing ratio
2. Other (potentially turbulence induced) factors outweigh the effects of flame speed.

Turbulent flame speeds are much harder to assess due to flames not having a relatively constant steady state to experiment on and the interaction of turbulence with other flame parameters [37]. The previously observed volatile nature of high mixing ratio turbulent flames with respect to a low mixing ratio equivalent flame is a possible cause or contribution to this phenomenon, however there is not enough data available to make definitive conclusions with respect to impact of turbulence yet.

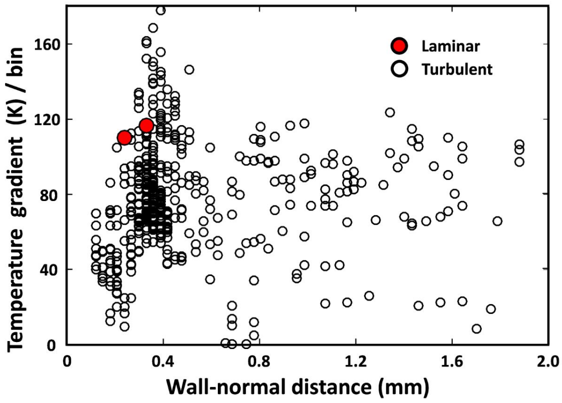

(a) Scatterplot of Temperature gradient with respect to the wall normal distance of each snapshot. Gradients are taken at the point where the temperature profile first reaches 1000K. The highlighted area marks all gradient exceeding the maximum observed in an equivalent laminar case.

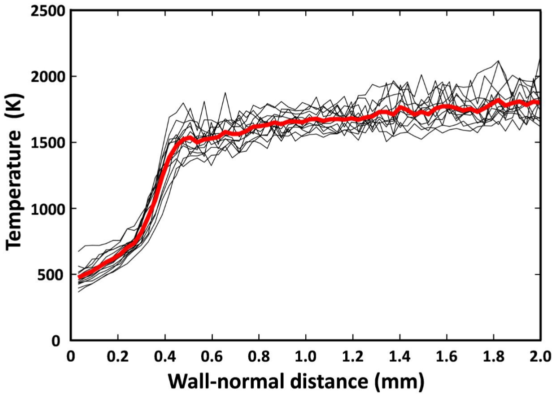

(b) Temperature profiles of all snapshots exceeding a temperature gradient of 120K/bin at the 1000K isotherm. Results obtained with a mixing ratio of 0.8.

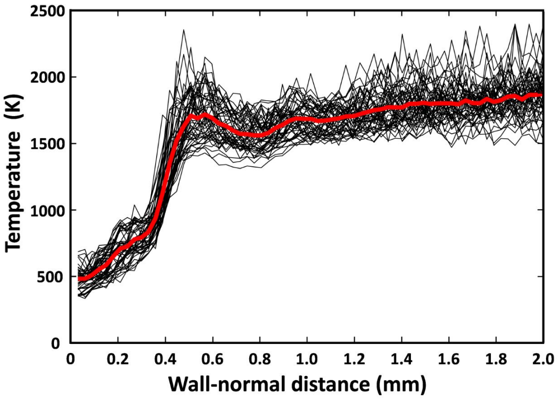

(c) Temperature profiles of all snapshots exceeding a temperature gradient of 120K/bin at the 1000K isotherm. Results obtained with a mixing ratio of 1.0.

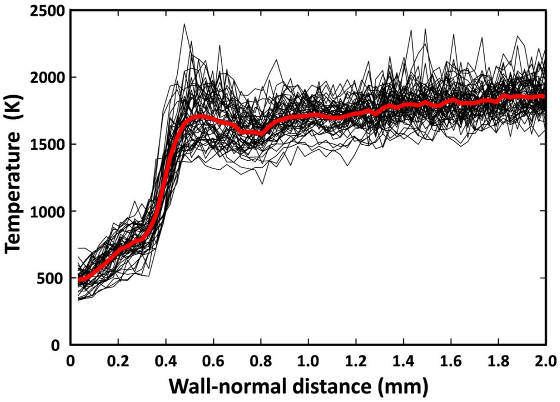

(d) Temperature profiles of all snapshots exceeding a temperature gradient of 120K/bin at the 1000K isotherm. Results obtained with a mixing ratio of 1.2.

Figure 5.8: Flame temperature gradient investigation of at the 1000K isotherm. Data points with gradients exceeding the maximum observed in an equivalent experiment on laminar FWI are isolated. The average of these data sets is marked with a red line and highlighted for each of the 3 equivalence ratios investigated.

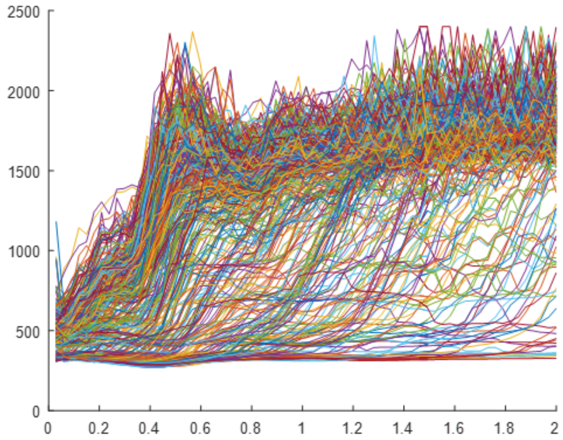

(a) Temperature profiles of a turbulent FWI in SWQ condition. Measurements taken with a stoichiometric mixing ratio at 52mm above the burner nozzle.

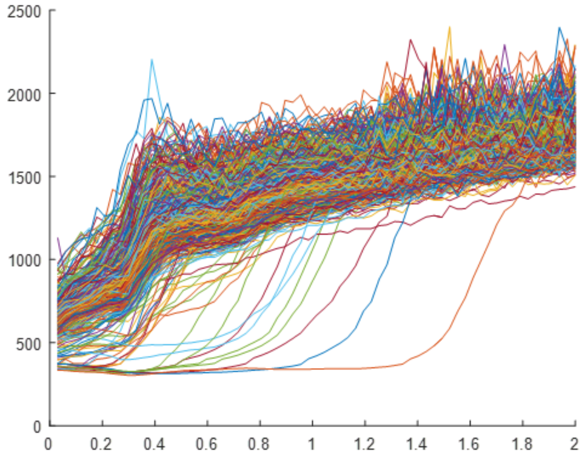

(b) Temperature profiles of a turbulent FWI in SWQ condition. Measurements taken with a stoichiometric mixing ratio at 58mm above the burner nozzle.

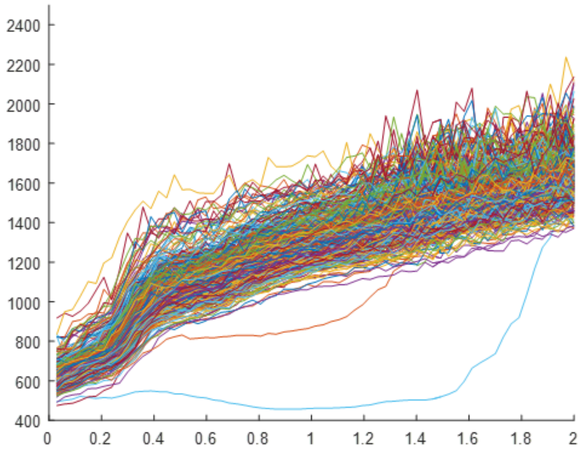

(c) Temperature profiles of a turbulent FWI in SWQ condition. Measurements taken with a stoichiometric mixing ratio at 64mm above the burner nozzle.

Figure 5.9: Temperature profiles of a turbulent flame in SWQ configuration measured at varying heights above the burner using CARS.

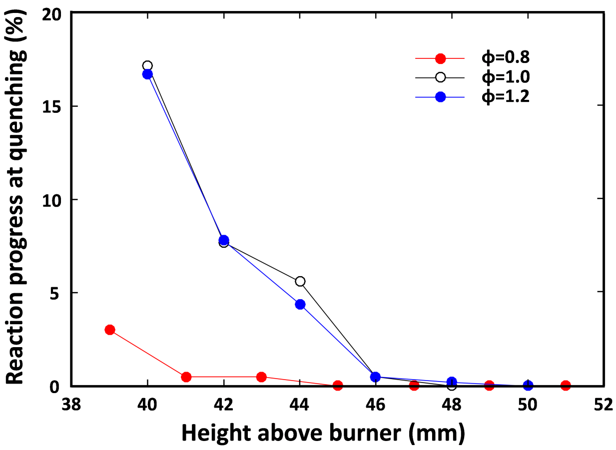

(a) Combustion progress variable with respect to height above burner for 3 mixing ratios: lean, stoichiometric and rich.

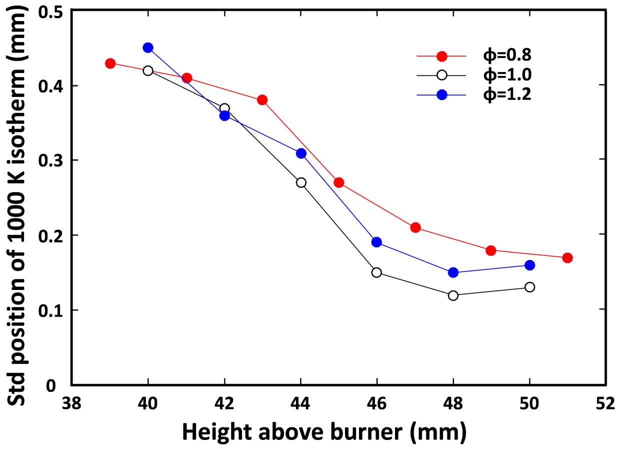

(b) Average distance to the wall of the 1000K isotherm with respect to height above burner for 3 mixing ratios: lean, stoichiometric and rich.

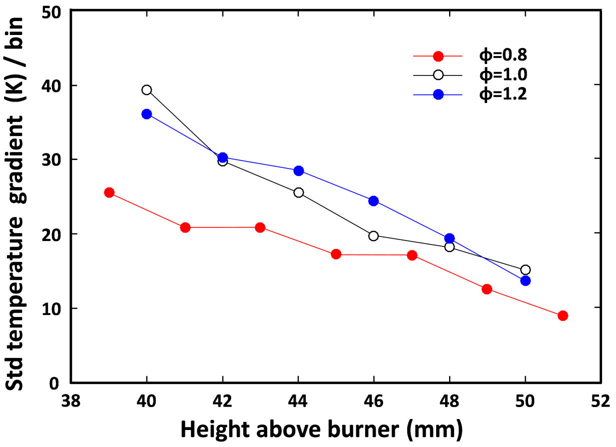

(c) Temperature gradient at the 1000K isotherm with respect to height above burner for 3 mixing ratios: lean, stoichiometric and rich.

Figure 5.10: Reaction progress, 1000K isotherm position and temperature gradient at 1000K isotherm with respect to the HAB for 3 mixing ratios: lean ($\phi = 0.8$), stoichiometric and rich ($phi = 1.2$).

6

EXPERIMENT

This chapter describes the experiment conducted for this thesis and presents its results.

6.1. SETUP

This section will firstly elaborate upon the dynamic range issue mentioned in the previous chapter. Subsequently, the method to investigate the issue is explained, followed by a description of the Matlab scripts used.

6.1.1. THE DYNAMIC RANGE OF A CAMERA

All cameras have a limited dynamic range. This range defines the maximum difference in intensities which can be captured in one shot. Due to the fact that advanced CARS techniques have been developed to make 1-D (line) measurements, a snapshot can be subjected to a much wider range of intensities than a single point measurement. While measuring along a line through the flame front provides a lot more useful information (especially with respect to FWI research), the information captured by this line usually contains signal data from both cold and hot regions. Since the CARS signal intensity scales is quadratically proportional to the number density, the colder regions (boundary layer at the wall, preheat zone, etc.) with a much higher density yield a much higher CARS signal intensity than the hot regions (i.e. flame front, oxidation zone, etc.). This prevents the camera from accurately capturing all the spectral data, which defeats the purpose of using CARS in the first place as one of it's prime advantages is the amount of information that can be captured in one shot.

Fortunately, a technique to combat this issue has already been developed: introducing a probe pulse delay. By delaying the probe pulse and giving the excited molecules some time to de-phase, the intensity difference between hot and cold areas can be reduced and the entire range of spectral data can be captured simultaneously. As previously mentioned when discussing the non-resonant background, this causes spectral heating. In order to account for this, the spectral libraries which are used to perform the spectral fitting need to be computed taking the probe delay into account. This thesis investigates whether or not the integrity of spectral libraries is affected by this and, if so, how much of a temperature error is caused by probe pulse delays in the spectral fitting routine.

In order to investigate the accuracy with respect to both pulse delay and temperature, a synthetic study has been conducted. Two scripts which have already been used to evaluate CARS data in previous experiments and were provided by Dr. A. Bohlin for this study, have been adapted to fit into a routine which generates a multitude of spectral libraries, each with a different probe pulse delay. Subsequently, a set of spectra is generated using the same script. The temperatures to which these spectra correspond have been chosen in the following manner: Firstly, a spectrum of the same temperature as the library temperatures is generated. In addition to this, 2 spectra corresponding to a slight temperature deviation (±1%) are processed in the same way for comparison. This highlights the sensitivity of the technique with respect to both probe pulse delay and temperature.

6.1.2. CODE STRUCTURE

The code used to conduct this study is based on the scripts described in chapter 5. The script used to generate the spectral libraries remains effectively unchanged, however a copy of this script has been altered and adapted to allow for more variation in the spectra that it computes. This mainly affected the measured linewidth library, which was measured in steps of 100K and hence had to be interpolated for all temperatures differing from the library entries. Another limit of this library is that the measurements only extend to the 41st rotational energy level. This has been mathematically extended in order to include 17 more energy levels. The intention is to further improve the accuracy of the spectral fitting routine by providing additional reference points. The linewidth values have been found to linearly decrease with increasing quantum number until a certain minimum is reached. The quantum number at which this limit is reached changes linearly with temperature and can thus be computed for library entries where this limit has not been recorded yet ($T > 1700K$).

In order to investigate the spectral library integrity with respect to probe pulse delay, the libraries computed use a probe pulse delay ranging from 50ps to 500 ps in steps of 10ps. The temperatures of the investigated spectra range from 300K to 2000K. In addition to the temperatures matching the library entries, the spectra for temperatures deviating by ± 1% have been computed for each of the probe pulse delays as well.

6.2. RESULTS

This section presents some of the results of the probe pulse delay investigation. Due to the amount of data points investigated, only a few select cases are presented here, the entire dataset can be found in Appendix A. The 4 different behaviour patterns found are displayed in Fig. A.3

Each figure displays the temperature error with respect to probe pulse delay for one of the investigated temperatures as well as their respective ±1% deviation temperatures. The temperature error is displayed on the y-axis in K, where a positive value implies the spectrum has been interpreted as hotter than it should be and vice versa. On the x-axis, the probe pulse delay in ps is shown.

The most notable thing is that the behaviour of the temperature error with respect to probe pulse delay does not seem to be consistent across the investigated temperature range. The following trends can be observed:

1. Graphs of 1700K and higher show little to no temperature error with respect to probe pulse delay. As the investigated temperature increases, the error steadily decreases.
2. While some temperature measurements are warmer than they're supposed to be, others are colder. This does not seem to follow a particular pattern however in both cases, the error increases steadily with probe pulse delay.
3. Especially at lower temperatures, a kink can be seen in the graph, particularly at lower probe pulse delay values. After a strongly irregular behaviour, the curve assumes a straight line again.

Table 6.1 summarises at which temperature which kind of behaviour is observed. Behaviours are classified as follows: A corresponds to a kink in the graph, B corresponds to a steadily increasing overestimation of temperature, C corresponds to a steadily increasing underestimation of temperature and D corresponds to a complete absence of temperature error. Graphs that show a kink usually resume regular behaviour afterwards and are therefore denoted with 2 categories.

Temperature in K	300	400	500	600	700	800	900	1000	1100
Error behaviour	A/B	A/C	A/B	A/C	B	C	B	B/C	C
Temperature in K	1200	1300	1400	1500	1600	1700	1800	1900	2000
Error behaviour	B	C/A	C	B	C	D	D	D	D

Table 6.1: Tabulated summary of essential experiment characteristics.

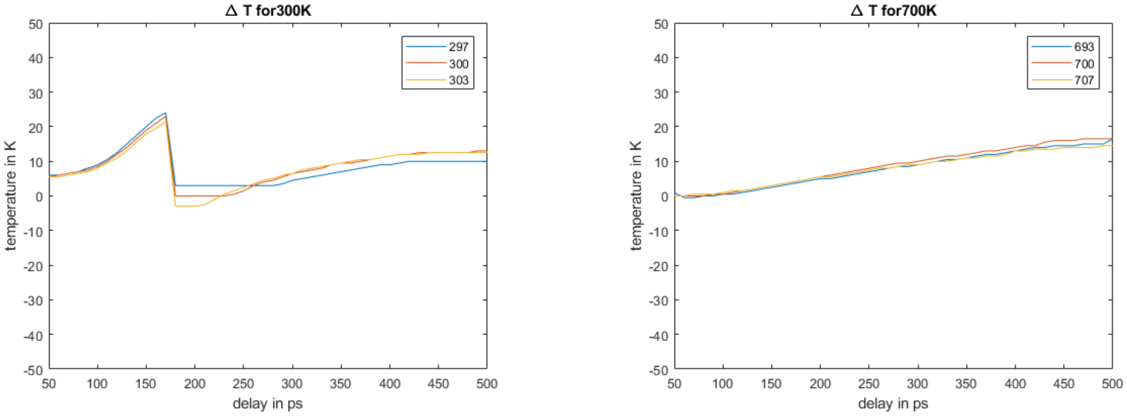

(a) 300K ± 1%

(b) 700K ± 1%

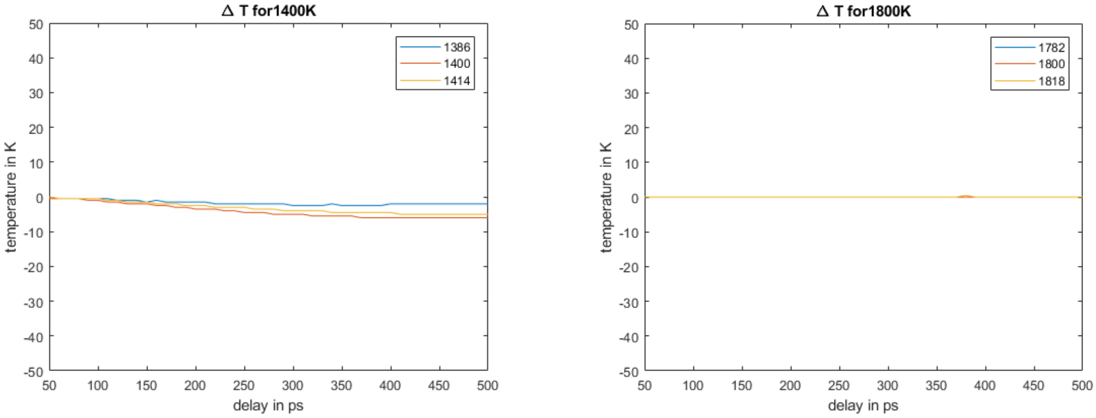

(c) 1400K ± 1%

(d) 1800K ± 1%

Figure 6.1: Temperature error with respect to probe pulse delay at 16 different temperatures.

There are 2 outliers to be found here, they can be found in Figure 6.2 Firstly, at 1000K, the trend initially seems to overestimate the temperature but around 250ps of delay, the slope of the graph flips downwards. This is the only temperature at which this occurs. The second outlier is at 1300K. This is the only temperature beyond 600K at which a strong kink is present in the graph. Additionally, unlike the other kinks, it occurs at a relatively high probe pulse delay (370ps for 1313 K and 430ps for 1300K). The curve for 1287K doesn't have a kink at all, making this the only data set where the 3 lines featured do not have a similar behaviour.

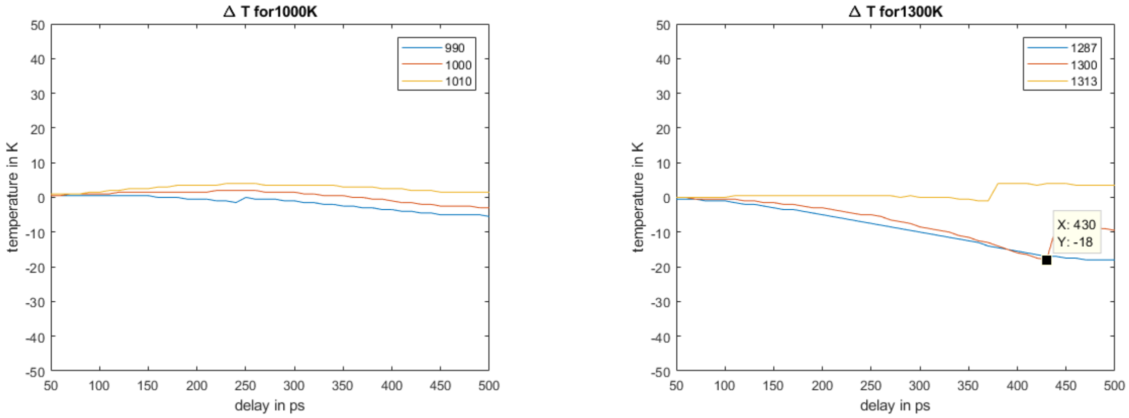

(a) 1000K ± 1%

(b) 1300K ± 1%

Figure 6.2: Temperature error vs probe pulse delay plots that show unique behaviour.

7

CONCLUSION AND RECOMMENDATIONS

A study has been conducted to establish the advantages of CARS as a thermometry technique for FWI research as well as investigate a possible source of inaccuracy. With the increase of information captured in a single snapshot, the finite dynamic range of the cameras used to capture the spectral data has become a limiting factor for the technique. By introducing probe pulse delays, the technique remains viable however the information captured by the camera has been altered in the process. By investigating the impact on the thermometry performance, future research can account and compensate for this effect, maintaining the accuracy of the technique. Specifically, the impact on spectral libraries used to interpret spectral data as temperature has been the focus of this study. The goal was to quantify the dependency of temperature errors caused by using a probe pulse delay with respect to the duration of the delay and the temperature of the observed probe volume.

Due to the otherwise continuous nature of the technique and the data generated, a continuous increase of the measurement error with delay was expected. However, the actual behaviour of the measurement inaccuracies appears to be discontinuous under the experimental conditions investigated throughout this thesis. The fact that the overall measurement error decreases with an increase in temperature fulfils expectations, as the main cause for delay induced inaccuracies is attributed to spectral heating. At higher temperatures, higher order rotational energy levels are populated, which have significantly lower de-phasing rates as their lower order counterparts. This reduces the overall signal decay with respect to time and, most importantly, the spectral heating effect since the majority of the populated energy levels have similar de-phasing rates. However, two aspects of the results obtained were unexpected and cannot be explained as of yet:

Firstly, the irregular behaviour which is primarily found at low temperatures. The kink in the temperature error graph (as shown in the example presented in fig. 6.1a) as well as one of the outlier graphs (fig. 6.2a) breaks with the otherwise continuous nature of the technique and the data generated by it. This raises the question whether the technique is viable to use at low temperatures or if there is another, previously unknown adverse effect on measurement inaccuracy which decreases with probe volume temperature.

Secondly, the fact that the continuous plots do not display either an increase of error with delay or a decrease, but appear to alternate between the two options. This suggests that another factor might be at play here which was not accounted for in the simulation.

It appears that spectral libraries are affected by the use of probe pulse delays, however more data on this effect is required in order to make accurate predictions for the temperature error. Future research conducted on this should be performed under the assumption that there are more dependencies than the flame temperature and the probe pulse delay, however since the probe pulse width has been kept constant throughout the entire study, this effect does not appear to originate solely from the input parameters.

While the results of the experiment conducted at Sandia National Research Laboratories hint towards several of the phenomena discussed in the FWI experiment review such as relaminarisation of the flow and flame front position fluctuations, an equivalent experiment on laminar FWI using a similar/identical setup would be required to obtain more definitive conclusions. By comparing this data to measurements of a laminar flame while thoroughly isolating any other contributions to temperature flux, a direct influence of turbulence on heat release in flames interacting with walls could be made. Moreover, irregularities encountered with respect to the introduction of a probe pulse delay merit a more detailed investigation of spectral library integrity. This investigation would need to focus solely on the data evaluation algorithms, however proper verification/ validation data would be required here as well. A thorough experimental setup as the one presented in this thesis (with exception of the turbulence grid) would serve the purpose of delivering the necessary information for both of these points and provide insight into both the difference between laminar and turbulent combustion as well as the influence of probe pulse delay on the accuracy of the overall technique.

CARS thermometry has been shown to be an accurate and precise tool which can be used to assess turbulent flames and, more specifically, turbulent FWI. Due to the limited understanding of the exact impact of turbulence on FWI and even combustion in general, an extensive investigation of flame turbulence using CARS is recommended to improve flame modelling and, subsequently, advance combustion technology to become more efficient and sustainable.

A

FIGURES

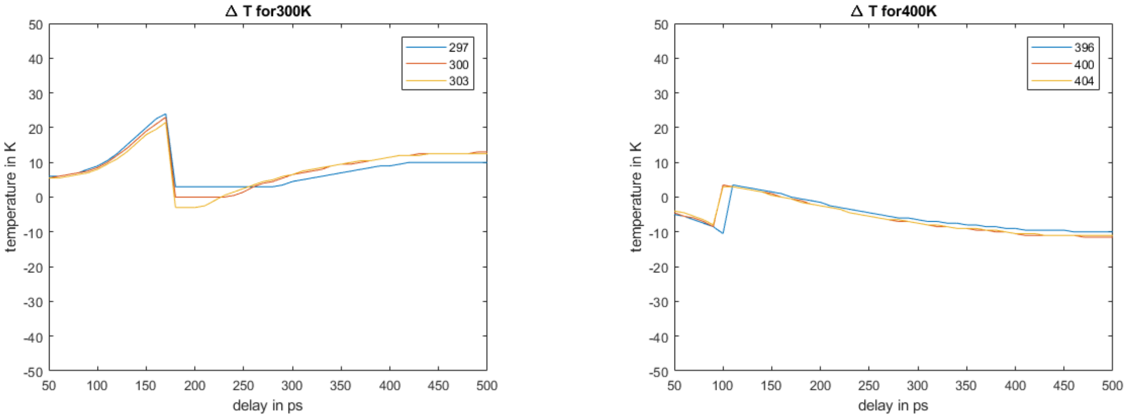

(a) 300K ± 1%

(b) 400K ± 1%

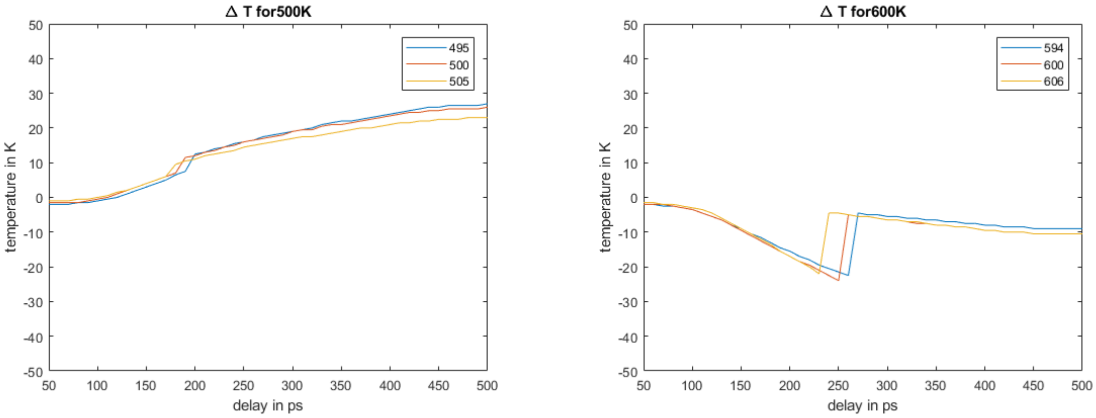

(c) 500K ± 1%

(d) 600K ± 1%

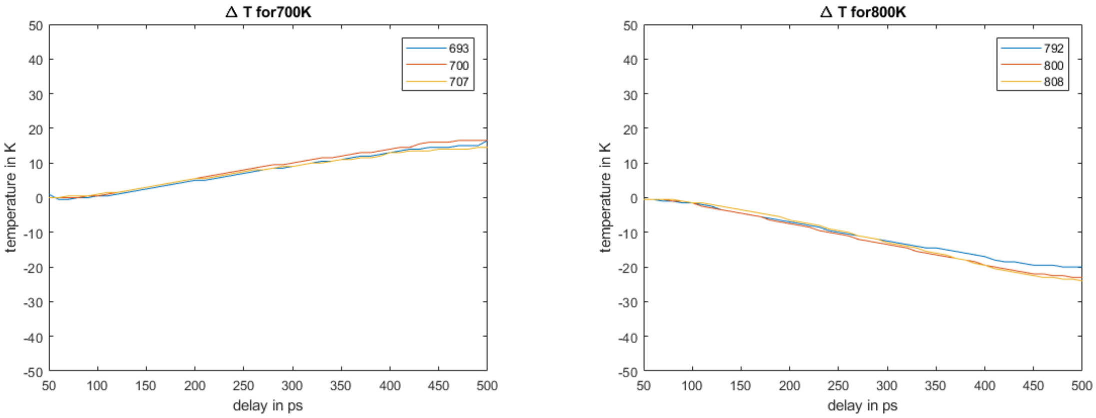

(e) 700K ± 1%

(f) 800K ± 1%

Figure A.1: Temperature error with respect to probe pulse delay, 300K - 800K.

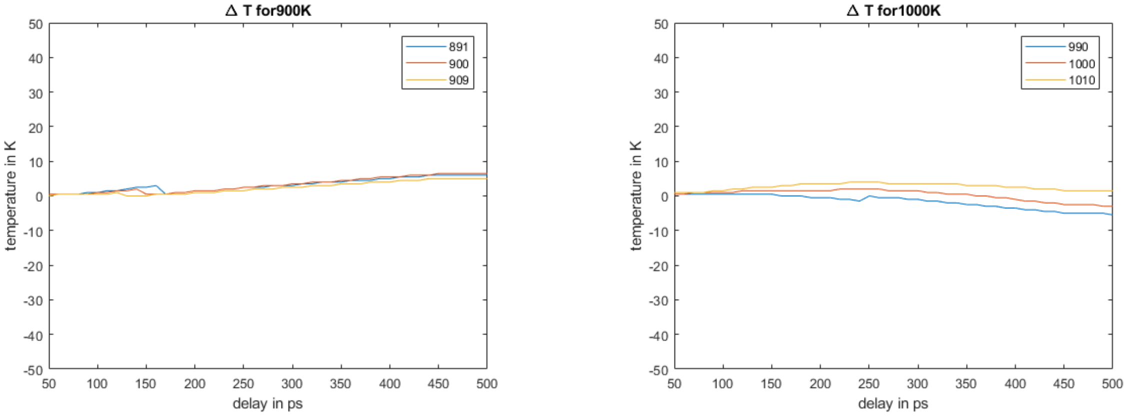

(a) 900K ± 1%

(b) 1000K ± 1%

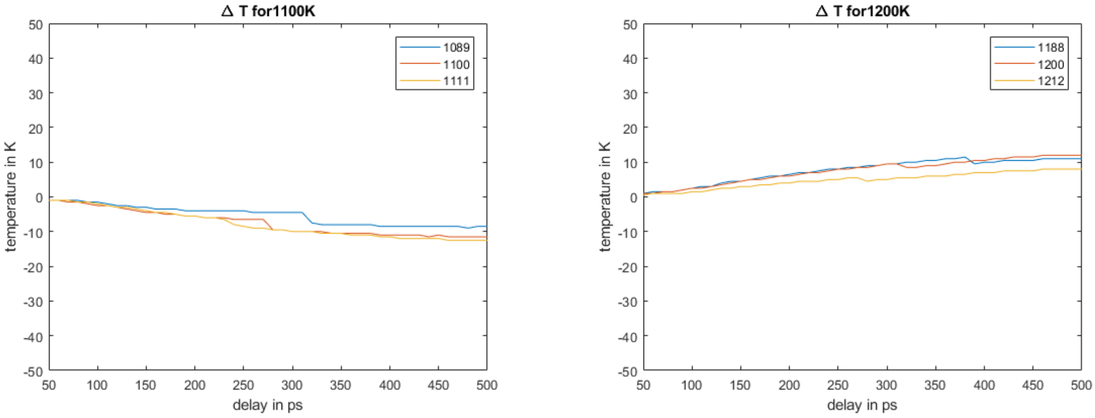

(c) 1100K ± 1%

(d) 1200K ± 1%

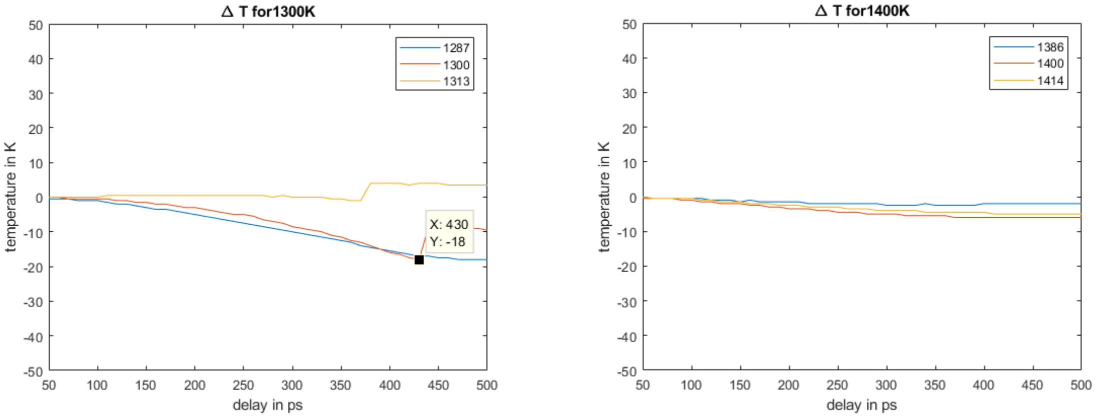

(e) 1300K ± 1%

(f) 1400K ± 1%

Figure A.2: Temperature error with respect to probe pulse delay, 900K - 1400K

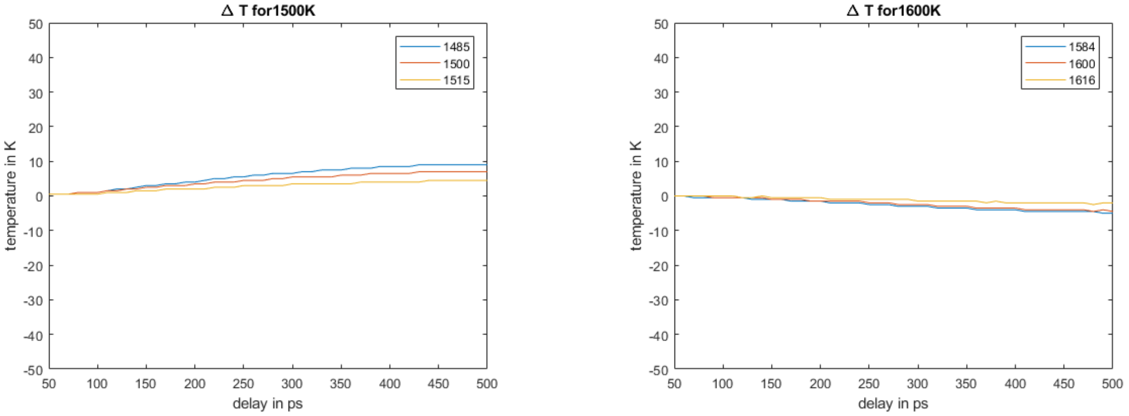

(a) 1500K ± 1%

(b) 1600K ± 1%

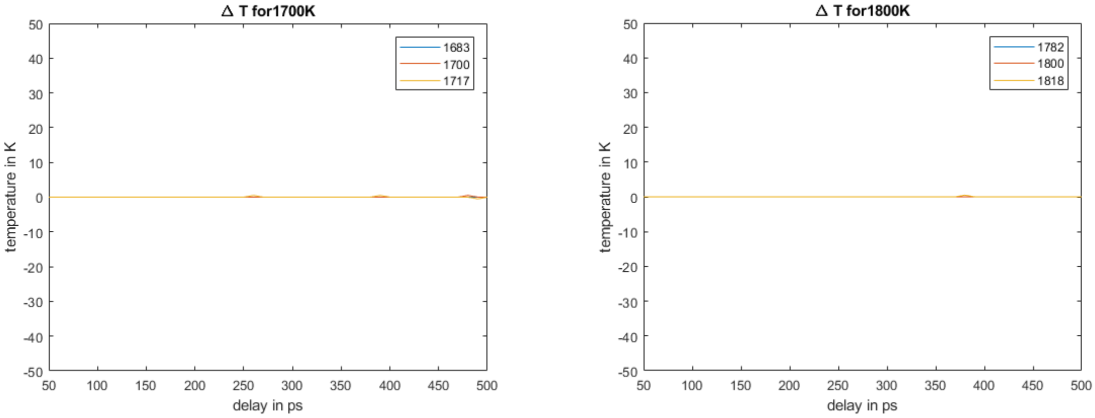

(c) 1700K ± 1%

(d) 1800K ± 1%

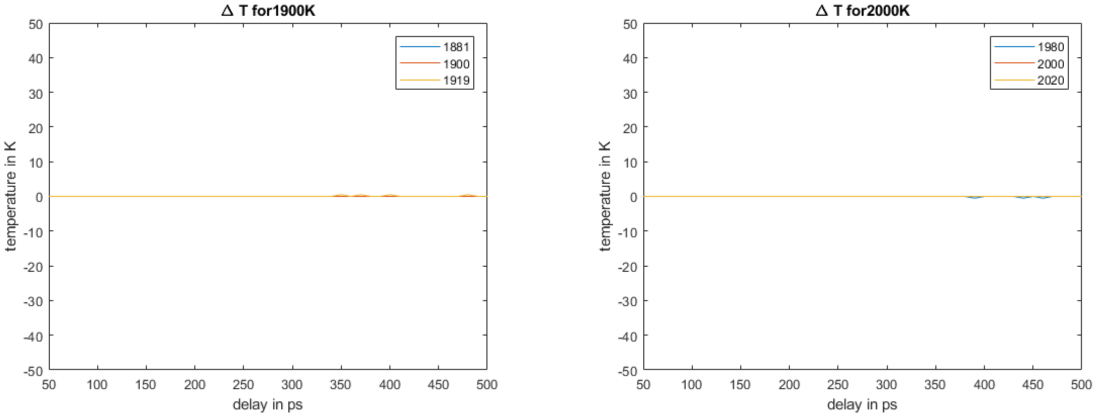

(e) 1900K ± 1%

(f) 2000K ± 1%

Figure A.3: Temperature error with respect to probe pulse delay, 1500K - 2000K

BIBLIOGRAPHY

[1] A. Dreizler, *Advanced laser diagnostics for an improved understanding of premixed flame-wall interactions,* Proceedings of the Combustion Institute **35**, 37 (2015).

[2] H. Sun, *High-pressure laminar flame speeds and kinetic modeling of carbon monoxide/hydrogen combustion,* Proceedings of the Combustion Institute **31**, 439 (2007).

[3] N. Syred, *The effect of hydrogen containing fuel blends upon flashback in swirl burners,* Applied Energy **89**, 106 (2012).

[4] H. Sun, *Turbulent flame speed as an indicator for flashback propensity of hydrogen-rich fuel gases,* Journal of Engineering for Gas Turbines and Power **135** (2013).

[5] L. M. Arin, *Reaction of ozone with carbon monoxide,* The Journal of Physical Chemistry **76**, 1514 (1971).

[6] H. Bockhorn, *Soot Formation in Combustion: Mechnism and Models* (Springer Verlag, 1994).

[7] L. C.K., *Combustion Physics* (Cambridge University Press, New York, 2006).

[8] V. Hoferichter, *Boundary Layer Flashback in Premixed Combustion Systems*, Ph.D. thesis, TU Munich (2017).

[9] C. T. Eichler, *Flame Flashback in Wall Boundary Layers of Premixed Combustion Systems*, Ph.D. thesis, TU Munich (2011).

[10] R. Suntz, *Two-dimensional visualization of the flame front in an internal combustion engine by laser-induced fluorescence of oh radicals,* Applied Physics B **47**, 287 (1988).

[11] S. Pfadler, *Flame front detection and characterization using conditioned particle image velocimetry (cpiv),* Optics Express **15** (2007).

[12] C. Jainski, M. Rißmann, B. Böhm, J. Janicka, and A. Dreizler, *Sidewall quenching of atmospheric laminar premixed flames studied by laser-based diagnostics,* Combustion and Flame **183**, 271 (2017).

[13] G. M. Baumgartner, *Flame Flashback in Premixed Hydrogen-Air Combustion Systems*, Ph.D. thesis, TU Munich (2014).

[14] S. Tachibana, *Flame front detection and dynamics using piv in a turbulent premixed flame,* (2018).

[15] A. Heinrich, S. Ganter, G. Kuenne, C. Jainski, A. Dreizler, and J. Janicka, *3D Numerical Simulation of a Laminar Experimental SWQ Burner with Tabulated Chemistry,* Flow, Turbulence and Combustion **100**, 535 (2018).

[16] E. Fernandez-Tarrazo, *A simple one-step chemistry model for partially premixed hydrocarbon combustion,* Combustion and Flame **147**, 32 (2006).

[17] A. H. Lefebvre, *Gas Turbine Combustion* (CRC Press, 1998).

[18] C. Bowman, *Kinetics of pollutant formation and destruction in combustion,* Progress in Energy and Combustion Science **1**, 33 (1975).

[19] M. O. Amdur, *Coal combustion aerosols and so2: An interdisciplinary analysis,* Environmental Science and Technology **20**, 138 (1986).

[20] G. Burton, *Chemical Ideas* (Heinemann, 2000).

[21] A. Bohlin, *Development and Application of Pure Rotational CARS for Reactive Flows*, Ph.D. thesis, Lund University (2012).

[22] A. Bohlin, *Single shot hyperspectral coherent raman planar imaging in the range od 0-4200cm-1,* Applied Physics Letters **105** (2014).

[23] A. Bohlin, *Multiparameter spatio-thermochemical probing of fwi advanced with coherent raman imaging,* Proceedings of the Combustion Institute **36**, 4557 (2016).

[24] D. R. Paschotta, *Understanding fourier spectra,* (2007).

[25] A. Bohlin, *Communication: Simplified two-beam rotational cars signal generation demonstrated in 1d,* The Journal of Physical Chmestry Letters **138** (2013).

[26] A. Laubereau, *Vibrational dynamics of liquids and solids investigated by picosecond light pulses,* Rev. Mod. Phys. **50**, 607 (1978).

[27] T. Seeger, *Picosecond time-resolved pure-rotational coherent anti-stokes raman spectroscopy for n2 thermometry,* Optics Letters **34** (2009).

[28] F. Grisch, P. Bouchardy, and W. Clauss, *Cars thermometry in high pressure rocket combustors,* Aerospace Science and Technology **7**, 317 (2003).

[29] V. Hoferichter, L. R. Boeck, G. Baumgartner, and T. Sattelmayer, *Flame Flashback in Hydrogen Combustion with Acoustic Excitation: Simultaneous PIV and OH PLIF Measurements at High Repetition Rate,* Fachtagung "Lasermethoden in der Stroemungsmesstechnik" (2014).

[30] A. B. A. Dreizler, *Detailed experimental investigation of thermo-kinetic and fluid mechanical properties of flame-wall interactions,* .

[31] M. Mann, *Transient flame-wall interactions: Experimental analysis using spectrosopic temperature and co concentration measurements,* Combustion and Flame **161**, 2371 (2013).

[32] C. Jainski, *Experimental investigation of flame surface density and mean reaction rate during flame-wall interaction,* Proceedings of Combustion Institute **36**, 1827 (2016).

[33] H. Kosaka, *Wall heat fluxes and co formation/oxidation during laminar and turbulent side-wall quenching of methane and dme flames,* International Journal of Heat and Fluid Flow **70**, 181 (2018).

[34] C. Jainski, *Quenching of premixed flames at cold walls: Effects on the local flow field,* Flow Turbulence Combustion **100**, 177 (2018).

[35] M. Rißmann, *Flame-flow interaction in premixed turbulent flames during transient head-on quenching,* Flow Turbulence Combust **98**, 1025 (2017).

[36] D. Zhu, F. Egolfopoulos, and C. Law, *Experimental and numerical determination of laminar flame speeds of methane/(ar, n2, co2)-air mixtures as function of stoichiometry, pressure, and flame temperature,* Symposium (International) on Combustion **22**, 1537 (1989).

[37] M. Huth and A. Heilos, *14 - fuel flexibility in gas turbine systems: impact on burner design and performance,* in *Modern Gas Turbine Systems*, Woodhead Publishing Series in Energy, edited by P. Jansohn (Woodhead Publishing, 2013) pp. 635 – 684.